Scientific Research Associates, inc.

P.O. Box 1058, Glastonbury, Connecticut 06033, Tel: (203) 659-0333

AD-A246 655

‖‖‖‖‖‖‖‖‖‖‖‖‖‖‖‖‖

Phenomena Unique to
Sub-Micrometer Devices

Final Report: R92-930033F; Contract: DAAH01-91-C-R184

Prepared by

H. L. Grubin, T. R. Govindan, B. J. Morrison and F.J. de Jong

DTIC
S ELECTE
FEB 2 4 1992
D D

For

Defense Advanced Research Projects Agency
3701 North Fairfax Drive
Arlington, VA 22203-1714

February 1992

Reproduction in Whole, or in Part, is Permitted
for any Purpose of the United States Government

92-04161
‖‖‖‖‖‖‖‖‖‖‖‖‖‖‖‖‖

92 2 18 177

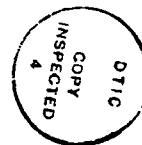# Final Report

12 February 1992

Sponsored by

Defense Advanced Research Projects Agency (DOD)

Defense Small Business Innovation Research Program

ARPA Order No. 5916

Issued by U. S. Army Missile Command Under

Contract # DAAH01-91-C-R184

Scientific Research Associates, Inc.
P. O. Box 1058
Glastonbury, CT 06033

P.I.: Dr. Harold L. Grubin
(203) 659-0333
Phenomena Unique to Submiron Devices

Effective Date of Contract: 1 August 1991
Contract Expiration Date: 10 February 1992
Reporting Period: 1 August 1991-10 February 1992

DISCLAIMER

REPORT DOCUMENTATION PAGE

1. AGENCY USE ONLY (Leave blank)	2. REPORT DATE	3. REPORT TYPE AND DATES COVERED
	920213	Final 1 Aug. 91 to 10 Feb. 92

4. TITLE AND SUBTITLE

Phenomena Unique to Sub-Micrometer Devices

5. FUNDING NUMBERS

C: DAAH01-91-C-R184

6. AUTHOR(S)

H.L. Grubin, T.R. Govindan, B.J. Morrison and F.J. de Jong

7. PERFORMING ORGANIZATION NAME(S) AND ADDRESS(ES)

Scientific Research Associates, Inc.
50 Nye Road
P.O. Box 1058
Glastonbury, CT   06033

8. PERFORMING ORGANIZATION REPORT NUMBER

R92-930033F

9. SPONSORING/MONITORING AGENCY NAME(S) AND ADDRESS(ES)

U.S. Army Missile Command
Redstone Arsenal, AL   35898

10. SPONSORING/MONITORING AGENCY REPORT NUMBER

11. SUPPLEMENTARY NOTES

12a. DISTRIBUTION/AVAILABILITY STATEMENT

Unclassified – Unlimited

12b. DISTRIBUTION CODE

13. ABSTRACT (Maximum 200 words)

An algorithm developed to solve the time dependent Liouville equation in the coordinate representation was implemented to examine phenomena unique to submicron structure. Quantum transport of electrons and holes in III-V and II-VI resonant tunneling structures was investigated. Attention was focused on the tunneling in and out of quantum wells by both electrons and holes. It was determined that characteristic transients including tunneling and capacitive contributions was of the order of one picosecond.

14. SUBJECT TERMS

Quantum Structure, II-VI Transistors, Tunneling, AlAs/GaAs

15. NUMBER OF PAGES

59

16. PRICE CODE

17. SECURITY CLASSIFICATION OF REPORT	18. SECURITY CLASSIFICATION OF THIS PAGE	19. SECURITY CLASSIFICATION OF ABSTRACT	20. LIMITATION OF ABSTRACT
Unclassified	Unclassified	Unclassified	UL

PHENOMENA UNIQUE TO SUB-MICROMETER DEVICES

Table of Contents

PHENOMENA UNIQUE TO SUB-MICROMETER DEVICES

THE PHASE I PROGRAM

Introduction

Historically, (a) the ability to reduce the size of electronic devices has resulted in both the exploration and the appearance of new device phenomena; and (b) the ability to predict new device phenomena has provided strong motivation for laboratory efforts to reduce device size. During the last decade this duality was manifested through the exploitation of velocity overshoot contributions. In the more recent past few years, and certainly in the coming decades, the exploitation of heterostructure materials growth has seen and will continue to see the development of a broad class of devices characterized by the confinement of charged particles. e.g., quantum wells, which confine electrons, holes and alter the spectra of phonons.

Quantum confined devices generally fall into two groups: (1) structures in which transport is *parallel* to the confining interfaces, e.g., HEMTs (see, e.g. Dingle, et al (1974) and Linh (1987), pseudomorphic HEMTs; and (2) structures in which transport in primarily *perpendicular* to the confining interfaces, e.g., resonant tunneling diodes (RTD) (Chang, et al. (1974)), hot electron transistors (see, e.g. Heiblum, (1981)), resonant tunneling bipolar transistors (Capasso and Kiehl (1985)). Recently, a third class of structures combined the essential features of parallel and perpendicular transport. These are represented by, e.g. the negative differential resistance FET (NERFET) (Kastalsky and Luryi (1983)), and resonant tunneling transistors (see, e.g., review by Capasso, et al. (1990)).

Device applications for parallel transport structures such as the HEMT have been pursued for a number of years, with initial emphasis on digital applications, and more recently on power applications. Device applications for perpendicular transport structures and perpendicular/parallel combination structures are only currently beginning to be addressed. As in the case of the more mature parallel transport technologies the *two specific issues identified with the newer devices are: (1) how much charge can be transported from one region of the structure to another region, and (2) how fast can the charge be transported from one region to the next?* Answering the dual questions of *how much and how fast* provides the basic guiding principles of device operation.

The Opportunity and Phase I Proposal

The establishment of guiding design principles for the operation of quantum confined devices is *necessary* for producing more functionality per unit area of chip. Such guiding principles require a quantum mechanically based set of equations that incorporate many particle statistics. Scientific Research Associates, Inc., (SRA) viewed this need as providing a major opportunity for introducing into the semiconductor device community, a work station based quantum mechanically correct algorithm that incorporates many-particle effects, electron and hole transport, and dissipation. SRA has developed an innovative quantum mechanical algorithm incorporating the above contributions which permits steady state computations to be completed in less than 15 CPU seconds on a CRAY, and less than 120 CPU seconds on a Silicon Graphics IRIS work station. This numerical breakthrough: (1) permits the exploration of phenomena that can significantly influence existing electronic device performance as the device is reduced in dimension, and (2) is capable of examining new and novel phenomena in ultra-submicron structures that can be used in new types of devices. SRA believes that its quantum mechanical work station configured algorithm will enable the use of its newly developed quantum mechanical algorithms to be used by the semiconductor community.

The purpose of the SRA, DARPA sponsored SBIR program, was to examine the combined issues of *how much and how fast* charge can be transported in perpendicular and combined perpendicular/parallel structures. The thread common to both types of structures is the ability of the quantum well to hold and release charge. *The quantum well is a leaky capacitor.* The program was structured such that during the first phase, perpendicular transport in one dimensional structures would be addressed; in an anticipated second phase, combined perpendicular/parallel transport in two dimensional structures would be considered. The program combines analysis with numerical simulations which rest on quantum mechanical algorithms developed at SRA.

The Innovation

Currently, the description of transport in quantum confined systems generally proceeds in one of three ways: (1) implementation of the Tsu-Esaki (1973) formulation, (2) implementation of the Wigner-Boltzmann equation (see, e.g., Frensley (1990)), and (3) implementation of the Liouville equation in the coordinate representation (Frensley (1985)).

The Tsu-Esaki formulation represents current through the formula:

$$J = [2e/(2\pi)^3] \int dk v(k) [f_{fd}(E) - f_{fd}(E + e\phi)] |T(E,\phi)|^2$$

Where f_{fd} is the equilibrium Fermi Dirac distribution function, $T(E,\phi)$ is the transmission coefficient obtained from solutions to the time independent Schrodinger equation, E is the energy of the particle and ϕ the applied potential.

The inadequacies of the above equation form the basis for the implementation of either the Wigner-Boltzmann equation or the Liouville equation, and are listed below:

• The Tsu Esaki formulation assumes equilibrium distribution functions, whereas there is strong evidence for hot electron effects in quantum wells and resonant tunneling structures (Goldman, et al. (1988)).

• The Tsu Esaki formulation ignores scattering. If hot carrier transport exists then strong carrier-carrier interaction, which is a scattering phenomena, is necessary.

• The Tsu Esaki formulation implies coherent processes in the quantum well. If strong carrier-carrier interaction occurs, transport contains significant incoherent contributions.

• The Tsu Esaki formulation is time independent. It is anticipated that important transient questions related to the filling and emptying of quantum wells cannot be answered within the framework of the Tsu-Esaki description.

Initial attempts to overcome the inadequacies of the Tsu Esaki formulation focused on implementation of the Wigner-Boltzmann equation. This is a quantum and statistically correct equation for describing transport. The Wigner Boltzmann equation has also been the subject of many numerical studies, with the emphasis placed on explaining resonant tunneling. Unfortunately, most practitioners of Wigner-Boltzmann algorithms have been faced with long computer runs, thereby limiting the use of the algorithms for examining the physics of quantum structure devices.

Less well known are studies involving solutions to the quantum Liouville equation whose solutions yield the density matrix. The implementation of the quantum Liouville equation was first proposed by Frensley (1985) who for unexplained reasons sustained numerical difficulties. Recent efforts at SRA (Govindan, Grubin and de Jong, (1991)) using "characteristic" algorithms developed by workers at SRA, have been successful at the study of quantum confined structures. *The innovation of*

the proposed program was the use of the density matrix in the coordinate representation for studying quantum confined systems.

Phase I and Phase II Program Goals

The *broad goal* of the program was to examine the switching speed of quantum feature size three terminal devices. Three structures are candidates; (1) the hot electron transistor, (2) the resonant tunneling gate FET, and (3) the more common pseudo-morphic HEMT. However, the goals of the Phase I program are more modest. These included demonstrating the feasibility of solving the quantum Liouville equation to determine transient switching times for III-V and II-VI configured heterostructure two terminal devices, incorporating electron and hole transport. Treating both III-V and II-VI configured heterostructures demonstrated that the SRA algorithm is not limited to a narrow group of semiconductor structures. Under the Phase I study it was proposed that the quantum Liouville equations, be applied to examining the filling and emptying of charge from the quantum wells under two distinct conditions: (1) the quantum well is filled with charge from an applied source, as in a resonant tunneling configuration, and (2) the quantum well is excited with electron-hole pairs. Two distinct systems were considered: the AlAs/GaAs double barrier system, and the HgCdTe/HgTe system. For the AlAs/GaAs a barrier configuration similar to that of Huang, et al. (1987) was chosen in which each barrier consisted of three 8.5Å AlAs undoped barriers separated by two undoped 8.5Å undoped GaAs regions. For this configuration the fact that the edge of the AlAs conduction band is an X point, whereas that of GaAs is a Γ point was addressed. For the II-VI structure, a double barrier structure consisting of a CdTe barrier, and a $Hg_{0.78}Cd_{0.22}Te$ quantum well was treated. Negative differential resistance from a single barrier with this latter composition was observed by Chow, et al (1988) at 4K.

An important feature of the proposed study was the further development of the quantum Liouville equation to incorporate more realistic models for treating dissipation for electrons and holes.

The specific technical objectives of the Phase I program are identified below.

Phase I Technical Objectives

Objective I. A key element of the Phase I program involving the switching characteristics of quantum confined structures, was the realistic incorporation of scattering elements into the algorithm. Thus one part of the study required further

inclusion and testing of scattering events for electron and holes into the SRA Liouville algorithm. *This objective was met.*

Objective II. For an AlAs/GaAs resonant tunnel diode subject to a bias that was sufficiently high to fill the quantum well with carriers, the objective was to successfully perform transient accurate calculations that incorporate scattering *with the goal of determining the time duration required for the valley current to be reached.* The unique features of this aspect of the study is the treatment of each undoped AlAs barrier as comprised of three 10 Å AlAs barriers separated by two 10 Å GaAs quantum wells; and addressing the issue that the conduction band edge of AlAs is at the X point whereas that of GaAs is at the Γ point. *This objective was partially met.*

Objective III. It is anticipated that a large number of quantum confined structures will involve the transport of electrons and holes. This is clearly the case under situations of photo-excitation of carriers. While a study of excess electron-hole generation and collection was not considered under this Phase I study, it is germane to the general properties of semiconductor devices to examine the relaxation of holes. A demonstration calculation was performed in which excess electron-hole pairs were placed in the resonant tunneling AlAs/GaAs diode. The objective was to demonstrate SRA's ability to successfully perform transient accurate calculations with the *goal of determining the time to relaxation. This objective was met.*

THE PHASE I STUDY

Introduction

The philosophy developed during the past few years with respect to the development of algorithms for examining phenomena in quantum based systems was that the algorithms must also be capable of explaining phenomena common to a wide variety of classical devices (superconducting devices are excluded). The ability to treat classical devices is crucial because it provides a benchmark by which the calculations can be tested. The calculations were tested subject to the constraint that under time independent steady state conditions the energy density applied to the structure is dissipated within the structure, as, e.g., identified in figure 1 for a simple system in which the device is part of a resistive DC circuit. The situation when time dependent self-excited oscillations (Shaw, et al. 1992) occurs, as in resonant tunneling applications, was not addressed.
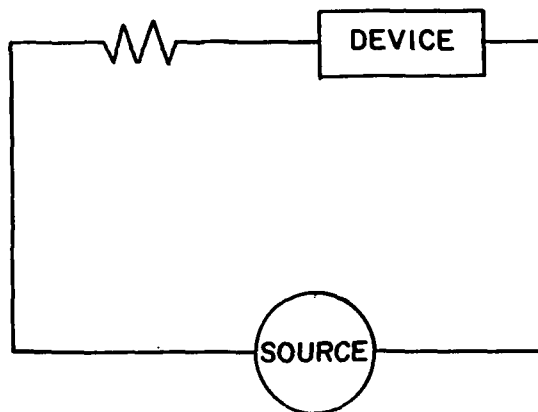

Figure 1. Schematic of the condition for calculating total current.

The way the condition of figure 1 manifests itself classically for a system of particles subject to an applied force and a frictional term proportional to momentum is that the steady state current is described by Ohms law: $\Phi = IR$, where Φ is the potential drop across the resistor.

The topics discussed below are germane to quantum structures. However to suitably place them in perspective we include a brief description of classical transport. This

discussion enables us to introduce the types of quantities that are calculated and the types of results that emerge from these calculations.

Conditions Necessitating Quantum Transport Algorithms

There is a hierarchy of equations describing device physics, see figure 2. For example a typical *classical analysis* of device problems involves developing and implementing algorithms for solving:

- the equation of continuity with generation and recombination
- the drift and diffusion equations (DDE) for electrons and holes, and
- Poisson's equation.

While the last decade has seen a explosion in the development of robust algorithms for solving these equations, device analysis bas~d upon them have been in the literature for over fifty years. Currently, DDE algorithms are implemented for solving transport and device design for III-V diodes, FETS and HBTs, etc. As is well known the *DDE are wholly inadequate for examining transport in structures whose features sizes are of the order of a mean free path, and whose frequency is of the order of the energy and momentum relaxation times of the carriers.*

The generic equations that are required for examining small feature size structures are identified in figure 2. As represented in figure 2 the drift and diffusion equations rest upon the Boltzmann transport equation (BTE) which, in turn, rests upon the fundamental quantum mechanical Liouville equation.
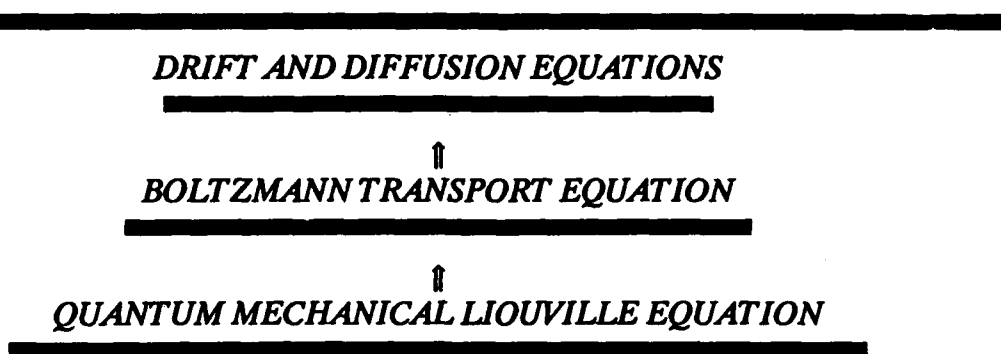

DRIFT AND DIFFUSION EQUATIONS

⇑

BOLTZMANN TRANSPORT EQUATION

⇑

QUANTUM MECHANICAL LIOUVILLE EQUATION

Figure 2. Hierarchy of Device Physics Equations.

How does the DDE describe device behavior, e.g., the generation and recombination of electrons and holes? As discussed above (shown below) this includes the continuity

equations for electrons and holes, and the rate equations for acceptor and donor traps. For example, with a single level of donors :

(1) $\quad \partial n/\partial t - \text{div}(j_n/e) = G + \{c_{nd}[n_d N_d{}^0 - n N_d{}^+]$

(2) $\quad \partial p/\partial t + \text{div}(j_p/e) = G + c_{pd}[p_d N_d{}^+ - p N_d{}^0]\}$

(3) $\quad \partial N_d{}^+/\partial t = -e_4 N_d{}^+ + e_1 N_d{}^0$

where superscripts denote ionized and neutral donors. The DDE equations are:

(4) $\quad j_n = -e[n v_n - D_n \text{grad} n],$

$\qquad j_p = e[p v_p - D_p \text{grad} p]$

and diffusivities are governed by the Einstein relation. The symbol G denotes the band-to-band generation of electron and holes as well as avalanche generation [4] is:

(5) $\quad G = (\text{band-to-band}) + a_n[\exp-(b_n/|F|)^m]|j_n| + a_p[\exp-(b_p/|F|)^m]|j_p|$

and the emissivity coefficients e_1, e_4 are: $e_1 = c_{nd} n_d + p c_{pd}$, $e_4 = c_{pd} p_d + n c_{nd}$. c_{nd}, c_{pd}, etc., are capture coefficients and include photoexcitation contributions; n_d, p_d, etc., are obtained at equilibrium. The above equations are coupled through Poisson's equation, which in terms of energy is:

(6) $\quad \nabla^2 E = -[e^2/\varepsilon][(n-p)-N_d{}^+]$

The energy and potential are related, $E = -e\phi$; the field in equation (5) is $F = -\nabla\phi$. *The output is current versus voltage versus illumination, and other related quantities, such as gain.*

The BTE description generalizes the DDE analysis. In the BTE analysis a distribution function f(x,p,t) is obtained as a solution to the BTE, from which all relevant quantities such as density, current density, etc., are obtained. The BTE for electrons is:

(7) $\quad \partial f/\partial t + (p/m)\cdot\nabla_x f - (\nabla_x V)\cdot\nabla_p f = [\partial f/\partial t]_{coll} + [\partial f/\partial t]_{g-r}$

f(x,p,t) is the probability of finding an electron at position 'x', with momentum 'p', at time 't'. The right hand side of equation (7) describes the interaction of the electrons with scattering events, generation and recombination events. 'V' is the

potential energy, which in the absence of heterostructures is obtained directly from Poisson's equation. With a suitable normalization, density, current density and energy density are:

(8) $n(x,t) = [2/h^3] \int d^3 p f(x,p,t),$

$j(x,t) = -e[2/h^3] \int d^3 p [p/m] f(x,p,t)$

$E(x,t) = [2/h^3] \int d^3 p [p^2/2m] f(x,p,t)$

with similar expressions for holes. In the device hierarchy, equation (7) with an equivalent one for holes replaces equations (1,2,4 and 5). Unfortunately, the BTE is inadequate for systems in which quantum effects dominant. The Liouville equation is needed.

The Liouville equation is a quantum mechanical operator equation. In commutator form, the equation is:

(9) $i\hbar \, \partial \rho_{op}/\partial t = [H, \rho_{op}]$

where ρ_{op} is the density operator and H is the system Hamiltonian. The Liouville equation is expressed with respect to a specific representation, the most popular being the *mixed representation* discussed by Wigner (1932). In the mixed representation the distribution function is the Wigner function and quantum transport is described by a differential equation that is *ostensibly* similar to Boltzmann equation and may be obtained from the latter by replacing the force term in equation (7) with (in one space and one momentum direction):

$+ (1/i\hbar)(1/2\pi\hbar)_{-\infty}\int^{+\infty} dp'_{-\infty}\int^{+\infty} dx' f(p',x')[V(x+x'/2,t)-V(x-x'/2,t)]\exp[i(p-p')x'/\hbar]$

An alternative representation is that implemented at SRA. The alternative representation is generally referred to as the *coordinate representation*; and the quantity computed is called the density matrix, which is related to the mixed representation (Wigner function) through (in one space and one momentum direction):

(10) $\rho(x,x',t) = [1/(2\pi h)]_{\infty}\int^{\infty} dp f(x,p,t)\exp[i(x-x')p/\hbar]$

In the DARPA sponsored SBIR study the density matrix equation of motion in the coordinate representation was solved for electrons and holes. In the following we will discuss this equation in stages. We will first write down these equations for

dissipationless systems, and introduce the notation to be used for the remainder of the discussion. This will be followed by a discussion of the relevant equations incorporating dissipation, followed by solutions to the problems studied.

Dissipationless Liouville Equation for Electrons and Holes

The Liouville equation in the coordinate representation for electrons (ignoring any spatially dependent effective mass and dissipation) is the following differential equation for electrons $\rho_e(x,x',t)$:

(11) $i\hbar\, \partial\rho_e/\partial t = -(\hbar^2/2m)(\nabla^2-\nabla'^2)\rho_e + [E_c(x,t)-E_c(x',t)]\rho_e$

The equation of motion of the density matrix is a *Schrodinger-like equation*. In its simplest form the density matrix for electrons can be obtained from a solution to Schrodingers equation through the relation:

(12) $\rho(x,x',t) = \Sigma\rho_{m,m}\psi_m(x,t)\psi^*_m(x',t)$

In equation (11) $E_c(x,t)$ is the conduction band energy that would appear in the single particle Schrodinger equation. $E_c(x,t)$ is obtained from the vacuum potential energy $V(x,t)$ from the Anderson rule:

(13) $E_c(x,t) = V(x,t)-X(x)$

where $X(x,t)$ is the electron affinity of the material. $\rho_e(x,x',t)$ is the density matrix for electrons in the coordinate representation.

The equation of motion of the density matrix for holes is:

(14) $i\hbar\, \partial\rho_h/\partial t = -(\hbar^2/2m)(\nabla^2-\nabla'^2)\rho_h - [E_v(x,t)-E_v(x',t)]\rho_h$

where $\rho_h(x,x',t)$ is the density matrix for holes in the coordinate representation. $E_v(x,t)$ is the energy of the valence band:

(15) $E_v(x,t) = V(x,t)-X(x)-E_g(x)$

and $E_g(x)$ is the bandgap energy.

All observables such as *density, current, energy,* are obtained from the *diagonal components* of the density matrix and suitable derivatives thereof, Grubin, et (1992). Thus the electron density is $\rho_e(x,x)$ and the hole density is $\rho_h(x,x)$:

(16) $\rho_e(x) = \rho_e(x,x)$

$\rho_h(x) = \rho_h(x,x)$

The potential energy of the vacuum is governed by Poisson's equation:

(17) $\nabla_x[\epsilon(x)\nabla V_x] = -e^2[(\rho_e(x) - \rho_h(x)) - (N_d^+(x) - P_a^-(x))]$

The background density in the above equation is assumed as a *jellium* doping distribution with N_d^+ representing the ionized donors and P_a^- representing the ionized acceptors.

Reduction of Liouville Equation for One Dimensional Spatial Transport

In the calculations described in this study we assumed Boltzmann statistics, spatial variations only along the x-direction, and free particle behavior along the y-and z-directions. The equation of motion of the density matrix was transformed to center of mass 'r' and nonlocal 'ζ' coordinates:

(18) $r = (x + x')/2,$

$\zeta = (x - x')/2,$

In these terms the density matrix is re-expressed as:

$\rho \Rightarrow \rho(r + \zeta, r - \zeta),$

and equation (11) for electrons becomes:

(19) $i\hbar \partial \rho_e/\partial t = -(\hbar^2/2m)\partial^2 \rho_e/\partial r \partial \zeta + [E_c(r + \zeta, t) - E_c(r - \zeta, t)]\rho_e$

with a comparable equation for the equation of motion of holes. In these variables Poisson's equation reads:

(20) $\partial/\partial r[\epsilon(r)\partial V/\partial r] = -e^2[(\rho_e(r) - \rho_h(r)) - (N_d^+(r) - P_a^-(r))]$

The diagonal components of solutions to equation (19) (along the diagonal $r = x$ and $\zeta = 0$) provide the density for the electrons with a similar description for the holes.

The Liouville Equation with Dissipation

The situation when dissipation is included results in a generalization of the equation

of motion of the density matrix. For electrons this becomes:

(21) $i\hbar\{\partial\rho_e/\partial t + [\partial\rho_e/\partial t]_{coll} + [\partial\rho_e/\partial t]_{g-r}\}$

$= -(\hbar^2/2m)\partial^2\rho_e/\partial r\partial\zeta + [E_c(r+\zeta,t)-E_c(r-\zeta,t)]\rho_e$

which is a *Schrodinger-like equation*, with a collision term. In the discussion that follows the mechanism of loss is Fokker-Planck dissipation. Strictly, this mechanism represents Brownian motion. As discussed by Calderia and Leggett (1983), the physics leading to this dissipation involves the system of electrons interacting with harmonic oscillators. It is not surprising that incorporating bulk phonons by the present authors, see appendix, resulted in contributions similar to that obtained by Claderia and Leggett (1983). In particular, in a limiting case Calderia and Leggett arrive at two terms associated with Fokker-Planck dissipation. The present authors have demonstrated that LO phonon-electron interaction leads to a term with the same gen~·⁻ form as the first term of the Fokker-Planck dissipation, discussed below ..m of the equation of motion of the density matrix in the presence of Fokker-Planck dissipation is:

(21) $i\hbar\partial\rho_e/\partial t = -(\hbar^2/2m)\partial^2\rho_e/\partial r\partial\zeta + [E_c(r+\zeta,t)-E_c(r-\zeta,t)]\rho_e$

$-(i\hbar/\tau)\zeta\,\partial\rho_e/\partial\zeta - [4iD\zeta^2/\hbar]\rho_e$

where 'τ' represents a relaxation time, and under classical conditions $D = mk_BT/\tau$. A similar equation exists for holes. Note, time independent steady state conditions, implies:

$\partial\rho_e/\partial t = 0$

The density matrix is Hermetian and equation (21) contains real and imaginary contributions. Recall that for current to be finite the wave functions from Schrodinger's equation must be complex. Similarly for current to flow the density matrix must be complex.

Observables

Current within the framework of the density matrix is a matrix:

(23) $j(r+\zeta, r-\zeta) = -e(\hbar/2mi)\partial\rho/\partial\zeta$

The observable is along the diagonal:

(24) $j(r) = -e(\hbar/2mi)\partial\rho/\partial\varsigma, @ \varsigma = 0$

Equation (24) has the same physical significance as the standard expression, equation (8), for current density.

Energy within the framework of the density matrix is matrix:

(25) $E(r+\varsigma, r-\varsigma) = -(\hbar^2/8m)\rho_{\varsigma\varsigma}$

The observable is along the diagonal:

(26) $E(r) = -(\hbar^2/8m)\rho_{\varsigma\varsigma}, @ \varsigma = 0$

Equation (26) has the same physical significance as the standard expression, equation (8), for energy density.

Analysis of Dissipation

Before proceeding with the analysis we describe our preliminary attempts at providing a means of quantifying the amount of dissipation occurring in the structure. Assume, for the sake of discussion that the potential energy expression appearing in the Liouville is differentiable; in which case the lead term in the expansion is:

(27) $E_c(r+\varsigma) - E_c(r-\varsigma) \approx 2\varsigma(\partial E_c/\partial r) + \ldots$

To this order and using the definition of current, the steady state time independent equation of motion of the density matrix becomes:

(28) $0 = -(\hbar^2/2m)\partial^2\rho/\partial r\partial\varsigma + 2\varsigma[(\partial E_c/\partial r)\rho - (m/e\tau)j] + [4D\varsigma^2/(i\hbar)]\rho$

The term in italics represents what we intuitively regard as an expression of classical momentum dissipation, when the diagonal components add to zero. For uniform applied fields where $\partial\rho/\partial r = 0$ and $\partial E_c/\partial r$ is constant, Ohms law emerges:

(29) $j = (e\tau/m)\rho dE_c/dx$

In the discussion that follows we have also found it useful for interpretive reasons to represent the current in terms of a quasi-Fermi energy:

(30) $j(r) = -(\tau/m)\rho(r)\partial E_f(r)/\partial r$

Introduction of the quasi-Fermi energy is an element in interpreting dissipation. For example, in discussions of resonant tunneling structures with the analysis obtained from the Tsu Esaki formulation, the current consists of two components, carriers coming from the cathode and carriers coming from the anode, each with a characteristic quasi-Fermi level. Because of the means by which the SRA algorithm selects carriers the density matrix incorporates both types of carriers. For carriers coming in from the anode the conduction band calculation is referenced with respect to an anode quasi-Fermi level. The value of the anode quasi Fermi level is chosen to yield a density in the anode region that is approximately equal to that of the background concentration.

The introduction of different cathode and anode Fermi levels represents a local equilibrium phenomena that arises because of scattering events. If all scattering events were included in the discussion, the introduction of the anode quasi-Fermi level would not be necessary. In the cases studied here dissipation was included, but the dissipation was introduced phenomenologically and taken as independent of position. All relevant dissipation mechanisms were not included. To compensate for this deficiency an *anode Fermi level* was introduced with the sole purpose of yielding a density on the anode boundary that was equal to background. The anode Fermi level contribution is represented by Σ_f. By way of comparison the quasi Fermi energy arising from the calculation is obtained from the solutions through the definition of equation (30) and is designated by the symbol E_f.

The argument of using the quasi Fermi level is justified, in the cladding regions, by assuming that the electrons are in local equilibrium with each other. If the carriers are also in local equilibrium with the lattice, then the distribution function in the cladding region will be Maxwellian with a quasi-Fermi level adjusted to assure that the carrier density is equal to the background concentration. Others, see, e.g., Potz (1989) have also assumed that the relaxation mechanism is to provide a distribution that represents local equilibrium and *eliminated the restriction that the carriers be in equilibrium with the lattice.*

In the absence of a general scattering term that incorporates carrier-carrier scattering and the details of electron-phonon scattering, the equation of motion of the density matrix was modified. In particular, the current contribution in the brackets of equation (28) is modified to read:

$$(31) \qquad 2m_\gamma j \Rightarrow 2m_\gamma j + \{\partial \Sigma_f / \partial r\} \rho$$

where Σ_f is specified. Note, equation (31) should be contrasted to equation (30), where the quasi-Fermi level is obtained *after* the calculation is completed.

SIMPLE EXAMPLES

Ohms Law

To see the kinds of results that the density matrix reveals we consider the first case of a uniform field structure subject to a constant relaxation time and particles entering with a displaced Maxwellian distribution.

For this calculation we examined a uniformly doped sample, $N_d^+ = 10^{18}/cm^3$, 1200 A long. Carriers enter the device subject to displaced Maxwellian boundary conditions. The equation of motion of the density matrix for electrons with Fokker Planck dissipation was solved along with Poisson's equation. The real and imaginary parts of the obtained density matrix are shown in figure 3. The real part provides the density, while the imaginary part provides the current.

The form of the density matrix for the simple case of Ohms law displays several characteristics that are common to all of the calculations discussed below. We first note that the real part of the density matrix is symmetric about the diagonal, and the imaginary part of the density matrix is anti-symmetric about the diagonal. These properties are consistent with the Hermetian property of the density matrix. With regard to the real part of the density matrix, its shape is gaussian. The gaussian is the density matrix representation of a Maxwellian distribution function (Feynman, 1972). In all of the calculations discussed below the carriers are entering with a gaussian distribution, and all features associated with any device structure appear within the center of the distribution function. The imaginary part of the density matrix has the form of a Gaussian multiplied by the term $\sin(2mv\zeta/\hbar)$, where 'v' is the local carrier velocity, and displays the asymmetry shown in figure 3. This asymmetry will also appear in all of the calculations at the edges of the structure.

The center of mass and nonlocal coordinates are identified in figure 3; and we point out that the density of the electrons is obtained from the diagonal component of the density matrix.

Because the field across this structure is constant the potential energy is a linear function of position. The calculation of figure 3 is for an applied bias of -10 mev. Figure 3b shows the distribution of potential, which was obtained from the solution of the density matrix coupled to Poisson's equation. The linear dependence is apparent. Because all of the dissipation is local, the quasi Fermi energy as computed from equation 30 follows the potential variation. This is also shown in figure 3b.

Real Part of the Density Matrix
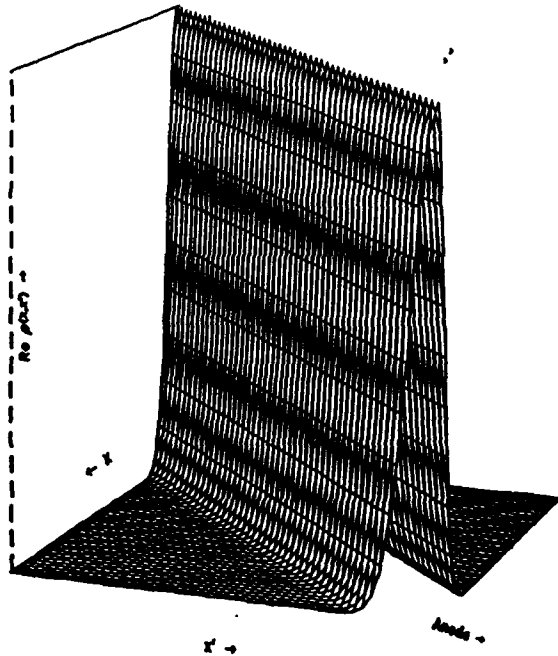
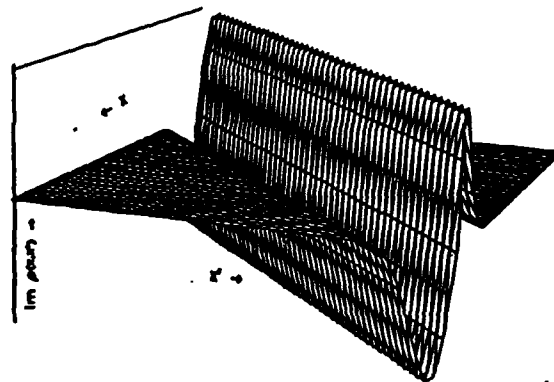Imaginary Part of the Density Matrix

Figure 3a. *Real and imaginary part of the density matrix corresponding to uniform fields and dissipation. The structure is 1200 Å long with a density of 10^{18} /cm³, subject to a bias of -10 mev.*
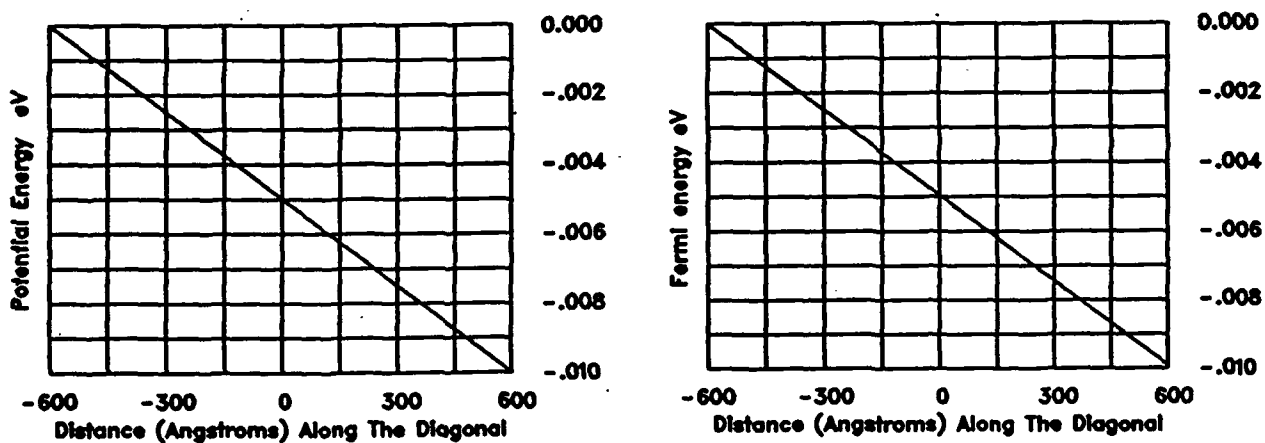
Figure 3b. *The potential energy and quasi-Fermi level for the computation of the uniform field condition of figure 3a.*

Space Charge Injection $N^+N^-N^+$ Structure

All of the double barrier calculations discussed below were incorporated into sandwich structures. To illustrate the types of results to be expected and to include the effects of dissipation and a discussion of the quasi-Fermi level, we examined a classical configuration. This calculation also exposes some of the incomplete features of the density matrix calculation as it now stands. *The incomplete features of the present algorithm are listed at the end of the discussion of results* section.

The $N^+N^-N^+$ structure studied is 1200 Å long with the center 250Å region doped to $10^{15}/cm^3$ and the cladding region doped to $10^{18}/cm^3$. Because of the small size of the N^- region the doping level is irrelevant, as the injected charge exceeds the background by several orders of magnitude. The equilibrium density matrix (zero bias) is shown in figure 4. Notice that the density matrix at the ends of the structure is the same as that of the uniform field calculation of figure 3, and reflects the Maxwellian character of the solution. The dip at the center of the density matrix represents the reduction in free charge density, and is associated with the N^- region. The reduction is charge is accompanied by an increase in potential energy. This is both the classical and quantum mechanical result, although in the latter the increase in potential is often referred to as an electrostatically generated barrier.

Real Part of the Density Matrix
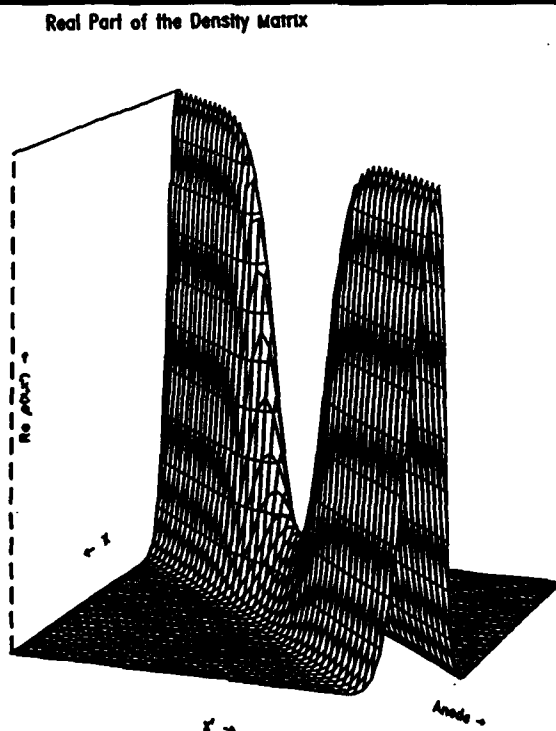
Figure 4. Equilibrium density matrix (real) for the $N^+N^-N^+$ structure.

The real and imaginary parts of the density matrix for a bias of -10 mev across the structure are shown in figure 5a. Note the apparent gaussian shape at the edges of the real part of the density matrix. For the imaginary part of the density matrix there is an increasing amplitude in the off-diagonal vicinity of the N⁻ region. Comparing the real parts of the density matrix at the anode side of the structure for both the equilibrium and biased cases it is apparent that there is some rounding of the anode charge density. Indeed the anode charge density is less than that at the cathode and reflects the incomplete dissipation model.

The potential and quasi-Fermi levels are shown in figure 5b, while the diagonal component of the density matrix, which is the density is shown in figure 5c. Also included in these figures are the equilibrium components. The density variation within the low doped region is not significantly different than the equilibrium solution. (For these calculations $\Sigma_f = \partial \Sigma_f / \partial r = 0$.)

The potential distribution reflects the presence of the electrostatic barrier. With regard to this distribution, we note that the relationship between the calculated field in the upstream cladding region and the current through the cladding region satisfy a local Ohms law relation.

Unlike the situation of uniform fields the quasi Fermi level does not follow the electrostatic potential. Rather it closely represents differences between the electrostatic potential in and out of equilibrium. The quasi-Fermi level decreases from the cathode to the anode and should, in principle, assume a value equal to that of the applied bias. In the absence of this result we have incomplete dissipation. The quasi-Fermi level is dependent upon the scattering rate and the applied bias. Indeed we are seeking conditions for choosing solutions to the density matrix that satisfy the condition that *all of the energy density applied to the system be dissipated within the system, and that this condition be consistent with constant values of density within the vicinity of the boundary.* Preliminary calculations indicate that this result can be achieved; but there was not sufficient time to incorporate this feature into the present study.

A calculation in which all of the energy *density* applied to the structure is dissipated within the structure was imposed for a bias of -20 mev. The results yield the correct value for the density on the anode contact, but the quasi-Fermi energy still exceeds that of the bias. (For these calculations $\Sigma_f = \partial \Sigma_f / \partial r = 0$.) These results are shown in figure 5.

Real Part of the Density Matrix
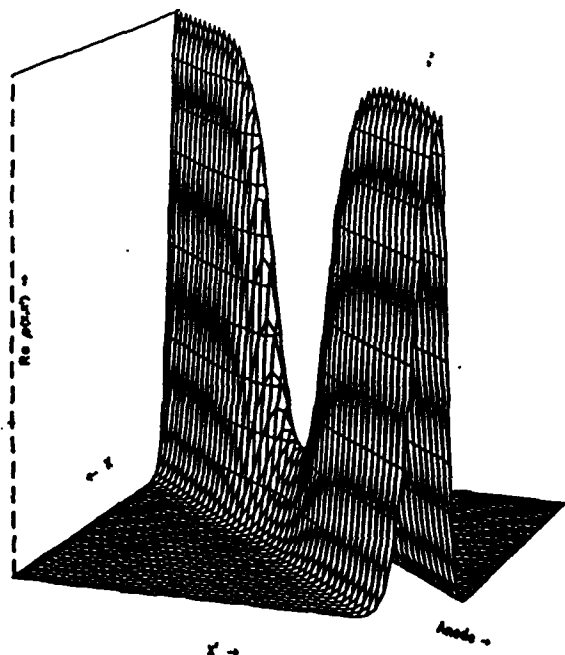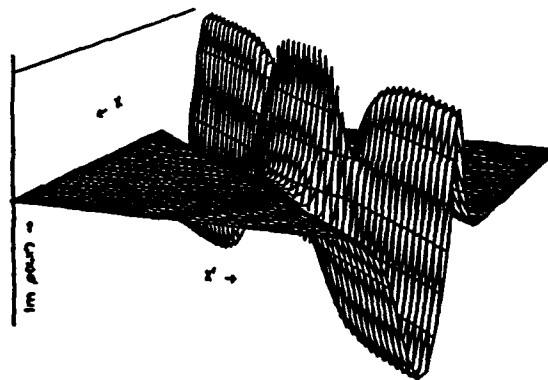
Imaginary Part of the Density Matrix

Figure 4a. Real and imaginary part of the density matrix corresponding to the $N^+N^-N^+$ structure with dissipation. The structure is 1200 Å long with a cladding density of $10^{18}/cm^3$, subject to a bias of -10 mev.
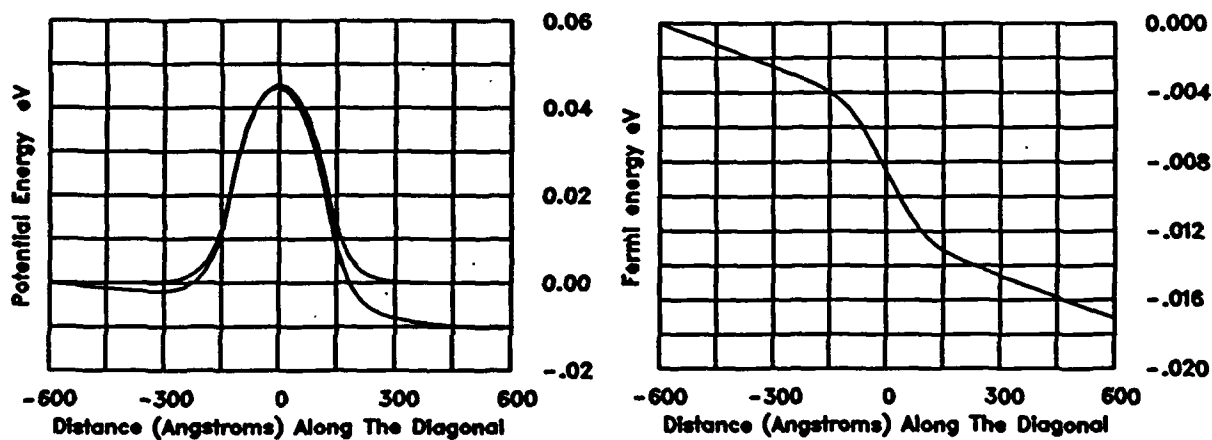
Figure 4b. The potential energy and quasi-Fermi level for the computation of the $N^+N^-N^+$ structure of figure 4a.
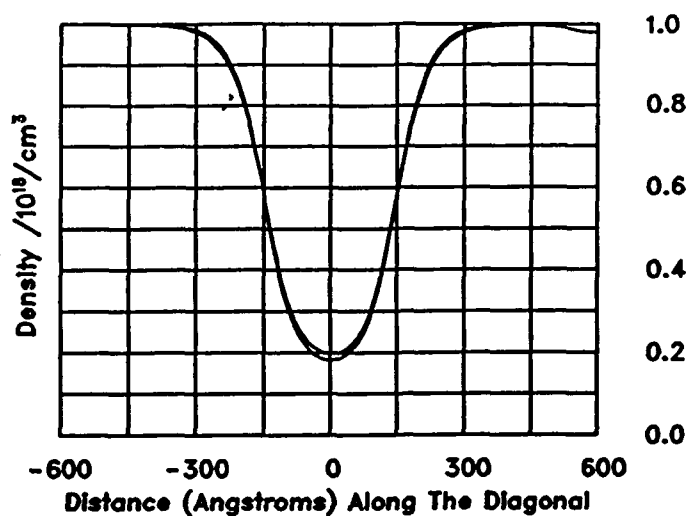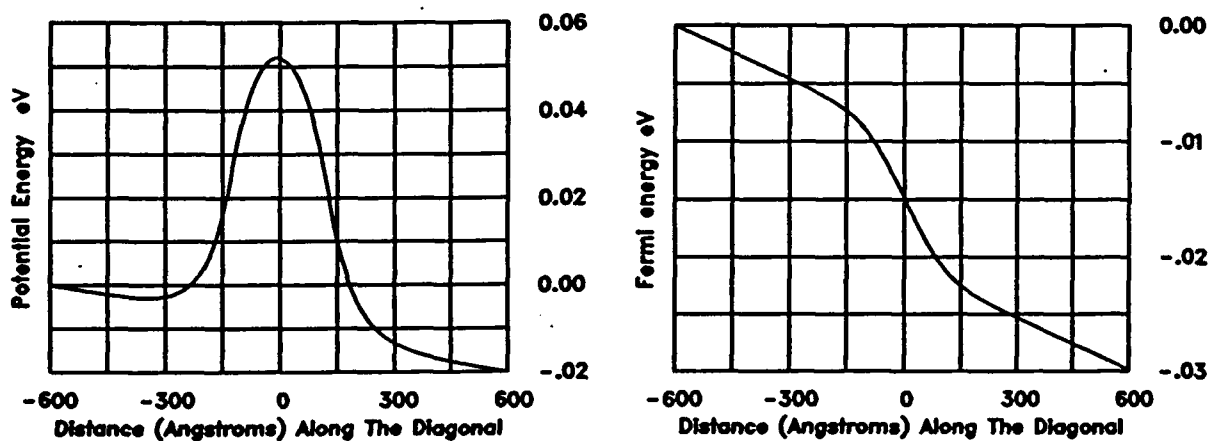
Figure 4c. The density distribution for the computation of figure 4a.

Figure 5a. The potential energy and quasi-Fermi level for the computation of the $N^+N^-N^+$ structure at a bias of -20 mev.
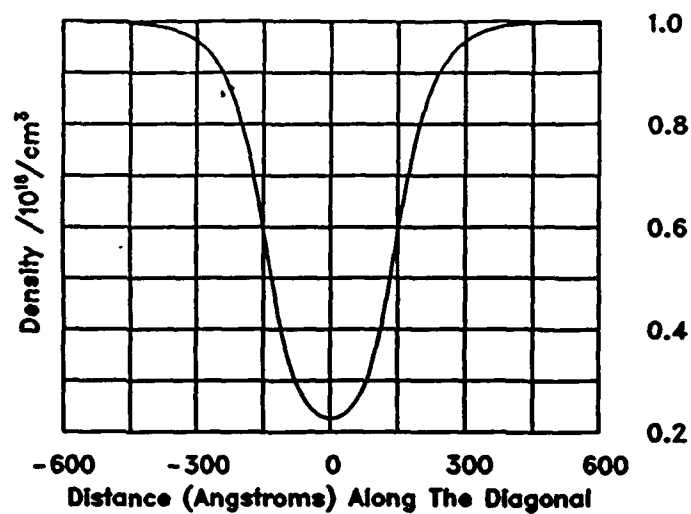
Figure 5b The density distribution for the computation of figure 5a.

RESONANT TUNNELING GaAs/AlAs STRUCTURES: STEADY STATE

The above calculations indicate some of the features to be explored in the study with the quantum structures discussed below. The first structure studied was the AlAs/GaAs resonant tunneling diode (RTD). These studies are of technological interest in that they yield high peak to valley ratios in the current voltage characteristics [Huang, et al. (1987)]. They also have interesting physical properties. For example, the band structure ordering of GaAs is Γ-L-X, whereas that of AlAs is X-Γ-L. Thus it may be anticipated that there will be some confusion as to the types of confinement to be expected. To illustrate this we examine figure 6, from Bonnefoi et al., (1988). Figure 6 displays a GaAs quantum well surrounded by two AlAs barriers. A variety of transport mechanisms can be envisioned. If transport is governed by the Γ valley carriers, then we are dealing with AlAs barriers of approximately one electron volt. If conduction is by the X valley carriers, and the X valley carriers have an effective mass considerably higher than the effective mass of the Γ valley carriers (as they would have in bulk material), then the barrier height to transport is reduced by approximately a factor of four. Another possibility is mixed conduction coupling Γ carriers in GaAs to barriers bound by the X valley in AlAs. In thermionic emission and photoluminescence studies of Dutta et al., (1989) of a GaAs/AlAs superlattice consisting of 50 periods of 39 Å GaAs and 57 Å AlAs, that X minimum instead of the Γ minimum in the AlAs layer was the relevant barrier height for transport in their experiment.

In the calculations below, we assume that the relevant barrier height to the Γ valley electrons is that of the X valley of AlAs. The calculations were performed assuming that each of the two barriers in the RTD consisted of three AlAs 10 Å barriers and two 10 Å GaAs wells. No variation in the effective mass was included in this study. The electron effective mass was taken as $0.067m_e$; the hole effective mass was taken as $0.45m_e$. For this structure no distinction is made between Γ and X, and the heterostructure is a type I category. .

AlAs/GaAs Under Equilibrium; N^- Region is 250 Å Long

For this calculation the donor concentration is the same as the $N^+N^-N^+$ calculation of figure 4. The acceptor concentration was taken to be uniformly equal to 10^{15}/cm^3. The equilibrium density matrix for electrons and holes is shown in figure 7a. The electron density matrix is different from that of figure 4 in two important ways. First, the density within the quantum structure is below that of the calculation of figure 4; second, a small excess charge in the quantum well is visible in figure 7a. The density matrix for holes displays three peaks and two valleys. The two valleys represent a reduction of hole density within the barriers. The middle
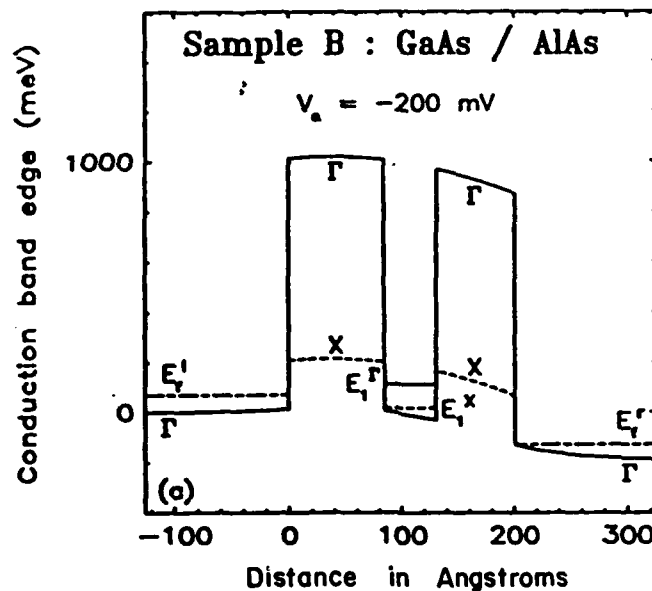
Sample B : GaAs / AlAs

$V_a = -200$ mV

Figure 6. GaAs/AlAs orientation for an RTD under bias. From Bonnefoi et al. (1988).

peak represents excess holes within the quantum well. The excess hole density outside the barriers appears in calculations in which the acceptor density is uniformly distributed. Similar results appear for comparably configured uniformly donor doped structures, Grubin et al (1992), where the excess charge has characteristics of Friedel oscillations.

Line plots of the equilibrium potential are shown in figure 7b. The elevation of the potential is a consequence of the low doped center region. Line plots of the electron and hole concentration are shown in figure 7c, and represent the diagonal components of the density matrix. Note the local increase in electrons and holes within the quantum well regions.

AlAs/GaAs RTD Under Bias: Electron Transport

The nonequilibrium situation under bias is considered in figures 8 through figure 11. These calculations assume only electron transport, the contribution of holes is considered later. For these calculations the constant relaxation time in the Fokker-Planck dissipation terms did not yield enough dissipation and the dissipation term was modified to include an additional quasi-Fermi level contribution.

Density Matrix of the Electrons

Density Matrix of the Holes
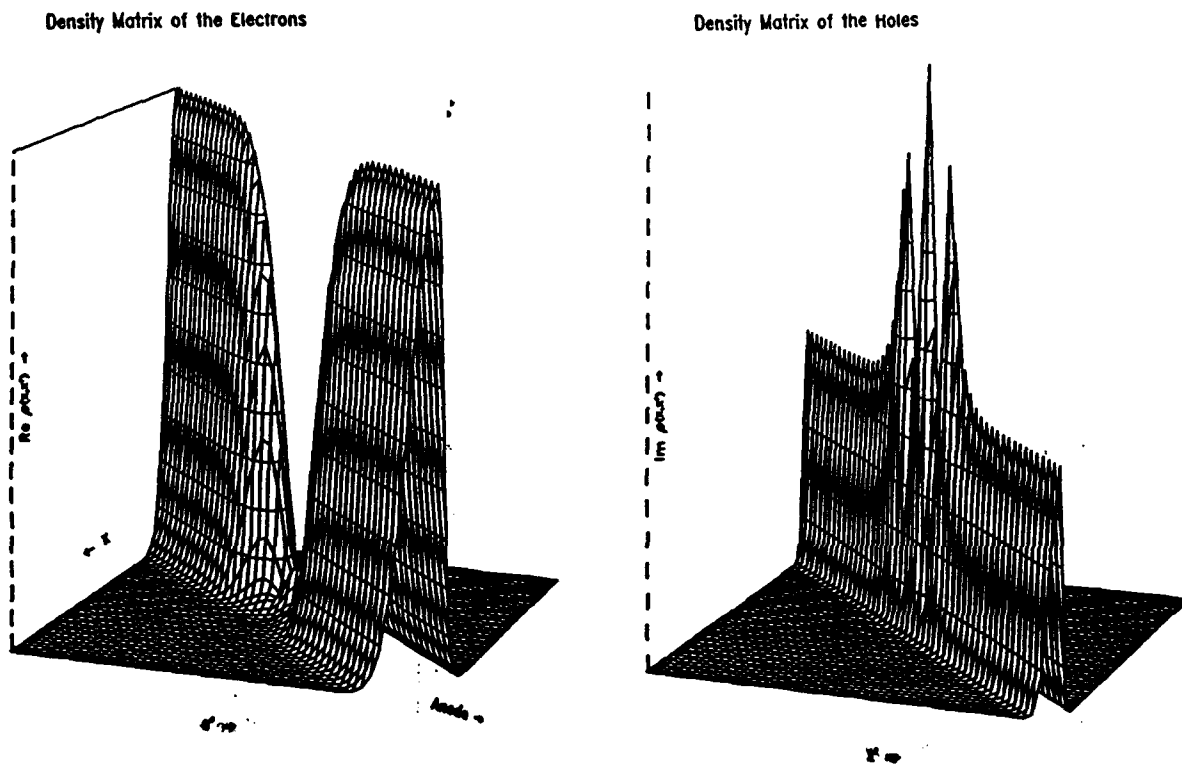
Figure 7a. Equilibrium density matrix for electrons and holes for the $N^+N^-N^+$ structure with AlAs/GaAs superlattice barriers.
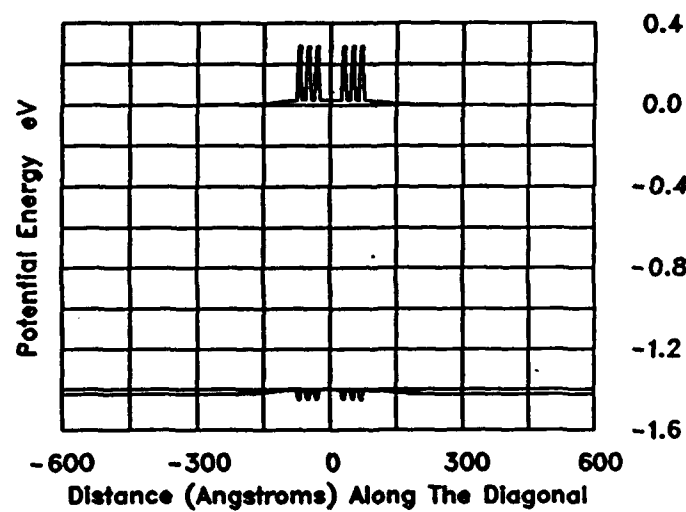
Figure 7b. The potential energy for the computation of figure 7a.
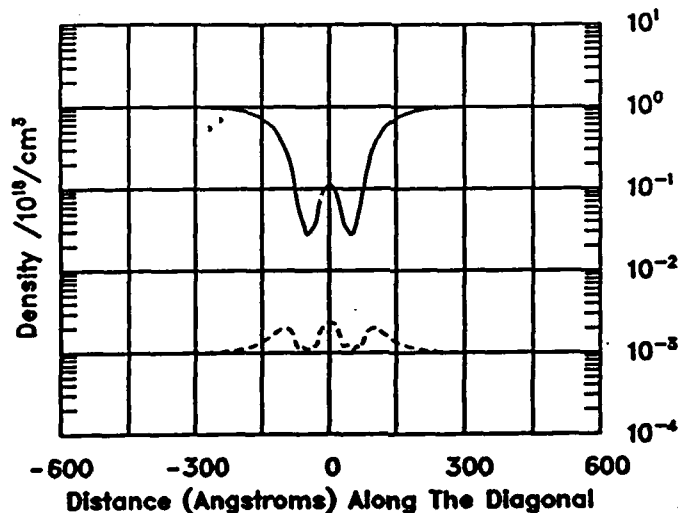
Figure 7c. The distribution of electrons and holes for the computation of figure 7a.

In the calculations below the mobility of electrons was taken to be 2600cm^2/Vs. The first set of calculations is for a bias of -100mev. The additional quasi-Fermi level Σ_f began at the beginning of the second barrier and was set equal to -75 mev. The calculated density, potential and calculated quasi-Fermi energy E_f are shown in figure 8. In figure 8a, the appearance of a finite and negative slope to the potential indicates the presence of a cathode field drawing electrons into the structure and generating current. There is also the beginning of a *notch* potential on the emitter side of the first barrier, attesting to local charge accumulation. The quasi-Fermi energy as computed from equation (30) is an estimate of the significance of dissipation on the distribution of carriers. The drop at the second barrier suggests its prominence.

Figure 8b displays a buildup of charge in the quantum well with depletion at the second barrier. Compared to the equilibrium calculation there is an accumulation of excess charge upstream of the first barrier, which is responsible for the notch potential, as well as within the first barrier. This excess charge distribution tends to reduce the potential drop across the first half of the structure, compared to the drop across the second half of the structure. The details are seen in the potential distribution for this calculation which displays a larger potential drop in the vicinity of the second barrier. In fact the potential drop across the second barrier is approximately equal to the potential drop across the first barrier and the quantum well. The quasi Fermi level distribution calculated from its *current* definition is shown in figure 8b. The current density for this calculation is 9.2x10^5 A/cm^2.
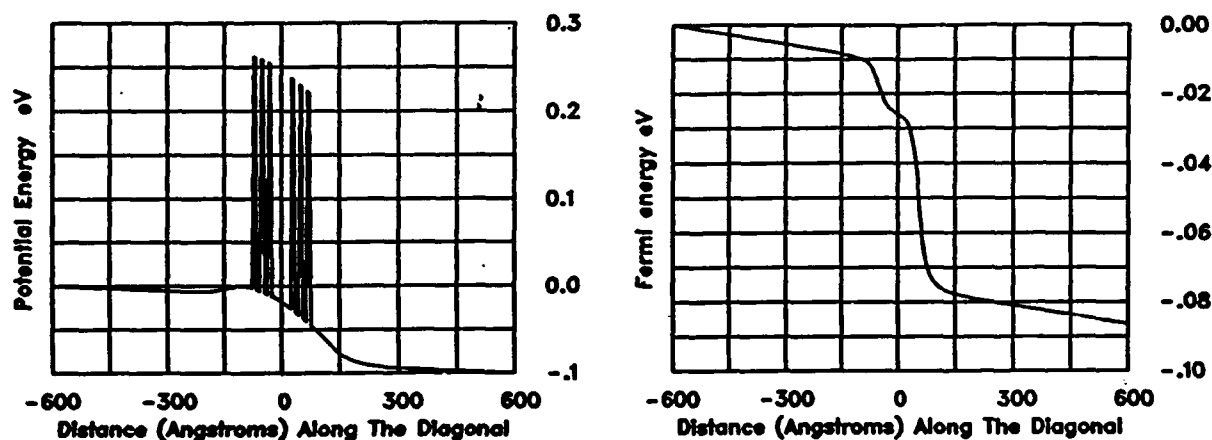
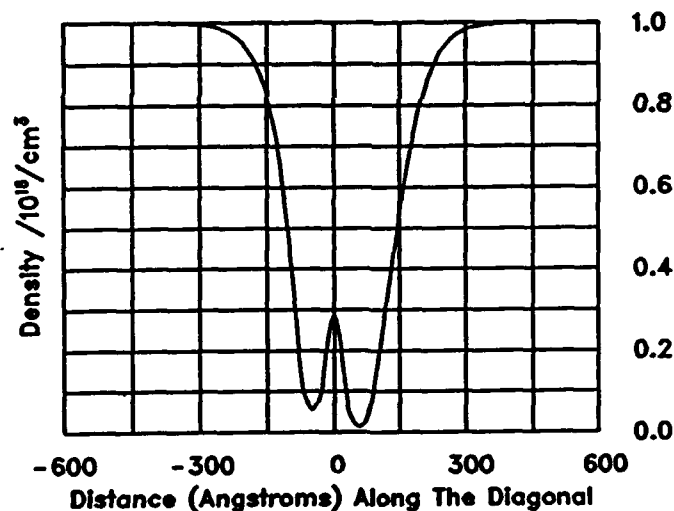*Figure 8a. Potential and Quasi-Fermi energy for the AlAs/GaAs RTD under a bias of -100 mev.*

Figure 8b. Density distribution for the calculation of figure 8a.

Consider next the situation at the higher bias of -200 mev. For this case $\Sigma_f = -90$ mev. The potential energy, and quasi Fermi energy are displayed in figure 9a; the charge density is displayed in figure 9b. We note that the charge density in both the quantum well and the upstream barrier is larger than the value at the lower bias case. There is no real change in the notch potential. The current increased to 2.8×10^6 A/cm² which is greater than a factor of three, as does the electric field at the upstream boundary.
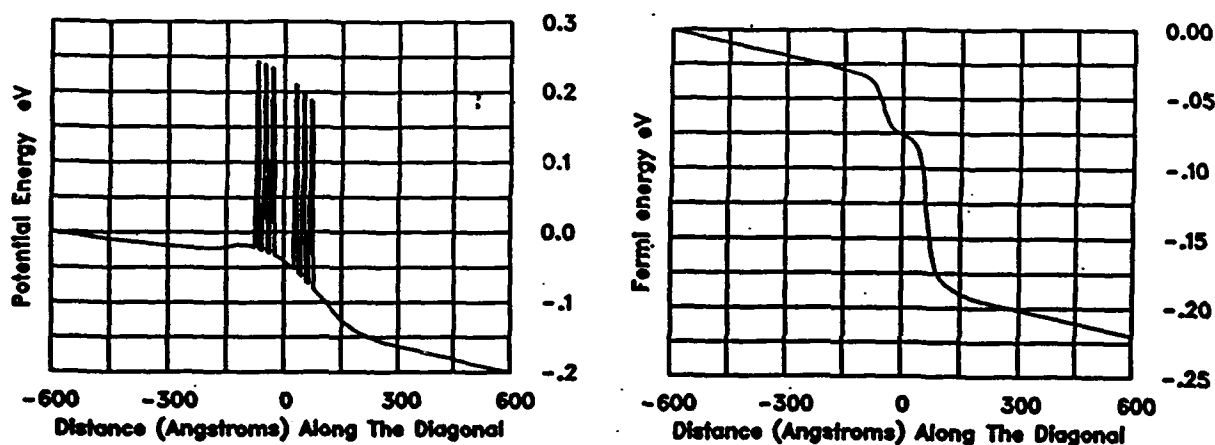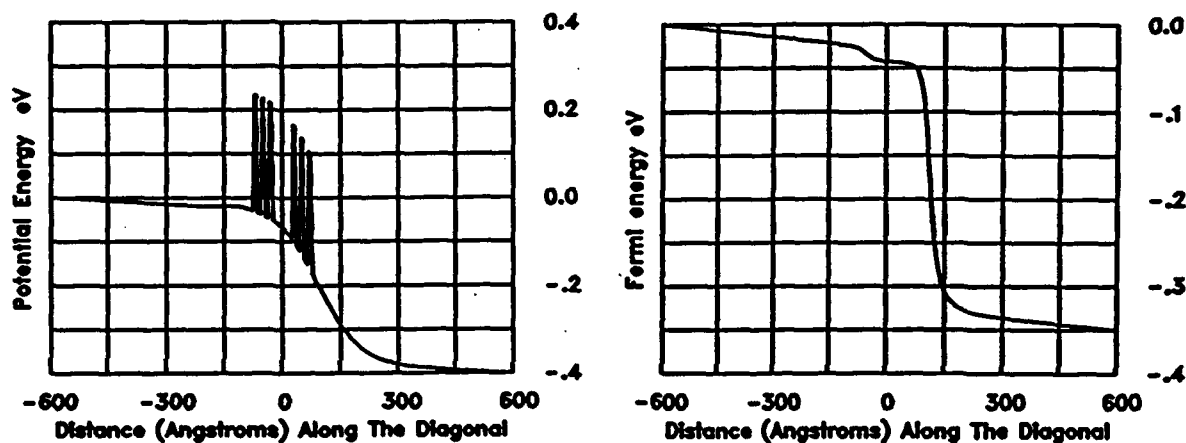
Figure 9a. Potential and Quasi-Fermi energy for a bias of -200 mev.
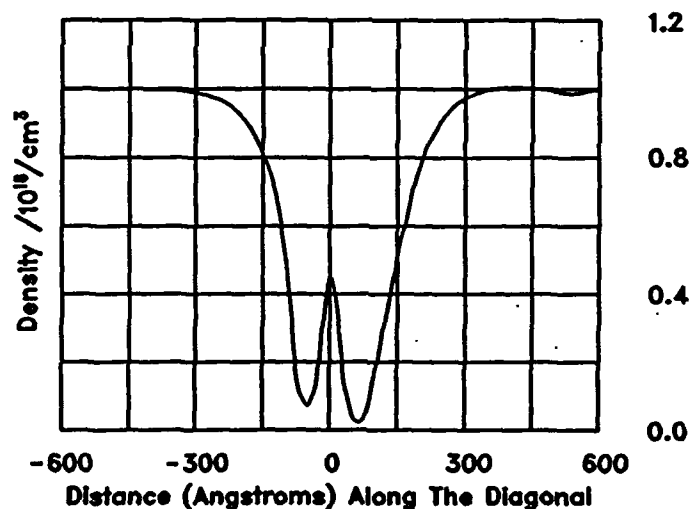
Figure 9b. Density distribution for the calculation of figure 9a.

With further bias increases there is a further increase in charge in the well, and increased region of charge depletion downstream of the second barrier, and a larger potential drop across the second half of the structure, then across the first half. In figure 10, we display the results for a bias of -400 mev, and $\Sigma_f = -325$ mev. But there is something qualitatively different here. First, the quasi bound state for the RTD

crosses the emitter Fermi level. There is both a high peak charge density within the quantum well, as well as considerable spread in the excess charge near and within the vicinity of the emitter barrier. The excess charge in the quantum well is accompanied by further depletion of charge within and downstream of the collector barrier. The calculated current for this case is 1.9×10^6 A/cm^2 and represents the fact that we are in the regime of negative differential conductivity. The onset of negative differential conductivity occurs at a bias level of somewhere between 200 mev and 300 mev. The current voltage characteristic is displayed in figure 11.

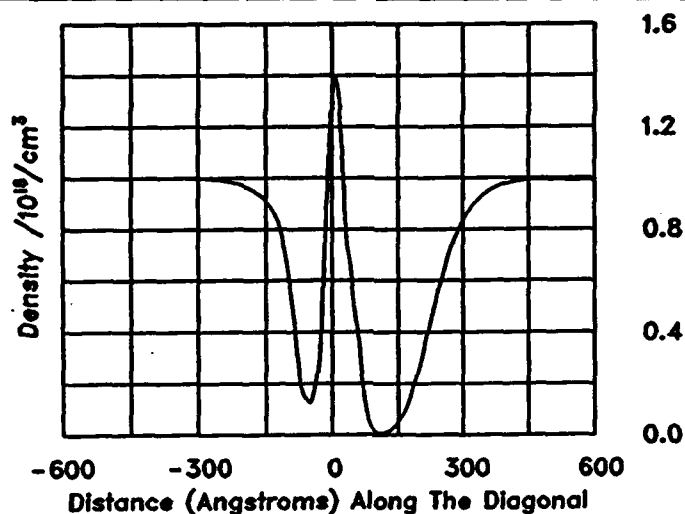*Figure 10a. Potential and Quasi-Fermi energy for a bias of -400 mev.*

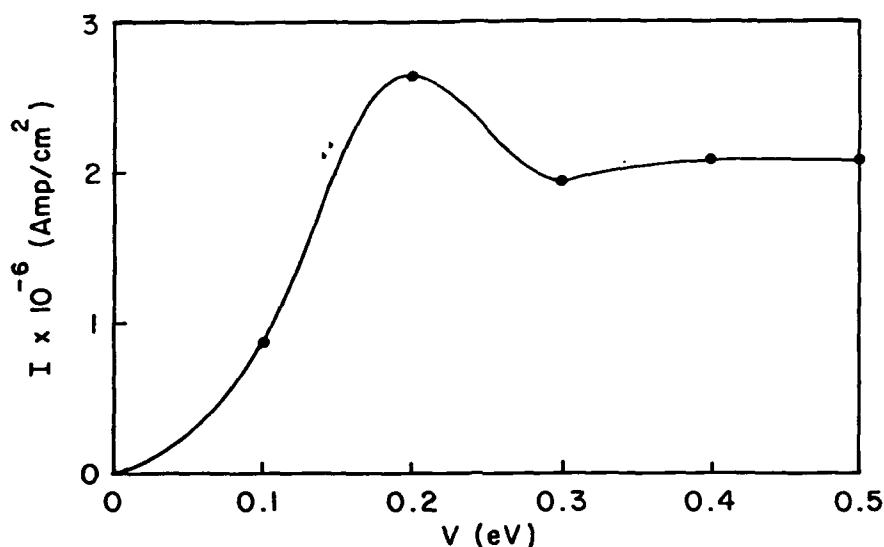*Figure 10b. Density distribution for the calculation of figure 10a.*

Figure 11. Current voltage characteristic for the calculations of figures 8 through 10.

Note that while the peak negative current occurs at 200 mev, we did not explore the actual peak position. It could occur before or after the value 200 mev. For this calculation the peak to valley ratio is 1.34. We point out that the current levels we are showing here are approximately a factor of two higher than that of Potz (1989), who dealt with AlGaAs/GaAs barriers. The large current density is a consequence of the mobility of the cladding region. We should be dealing with a mobility that is significantly lower.

AlAs/GaAs, the N^- Region is 500 Å Long

The above calculations were repeated for the case of a wider cladding region. The N^- region was increased to 500 Å. The potential and charge distribution at equilibrium, at -200 mev where the current peaks, and at 300 mev are shown in figure 12. There are several points to note: *First*, as the bias increases the amount of charge in the well increases. This is a feature that also appears in the calculations with the narrow N^- region. *Second*, there is a buildup of charge upstream from the first barrier that tends to pin the emitter side of the barrier at zero volts. *Third*, there is a much more dramatic appearance of a notch potential for this calculation. This is a direct consequence of the doping configuration. *Fourth*, there is much less potential drop across the first barrier. This is a consequence of the excess charge in the quantum well that tends to screen the first barrier from the applied bias. *Fifth*, the voltage distribution beyond the peak current corresponds to a quasi bound state that is somewhat above the emitter Fermi level, but below the ground state of the
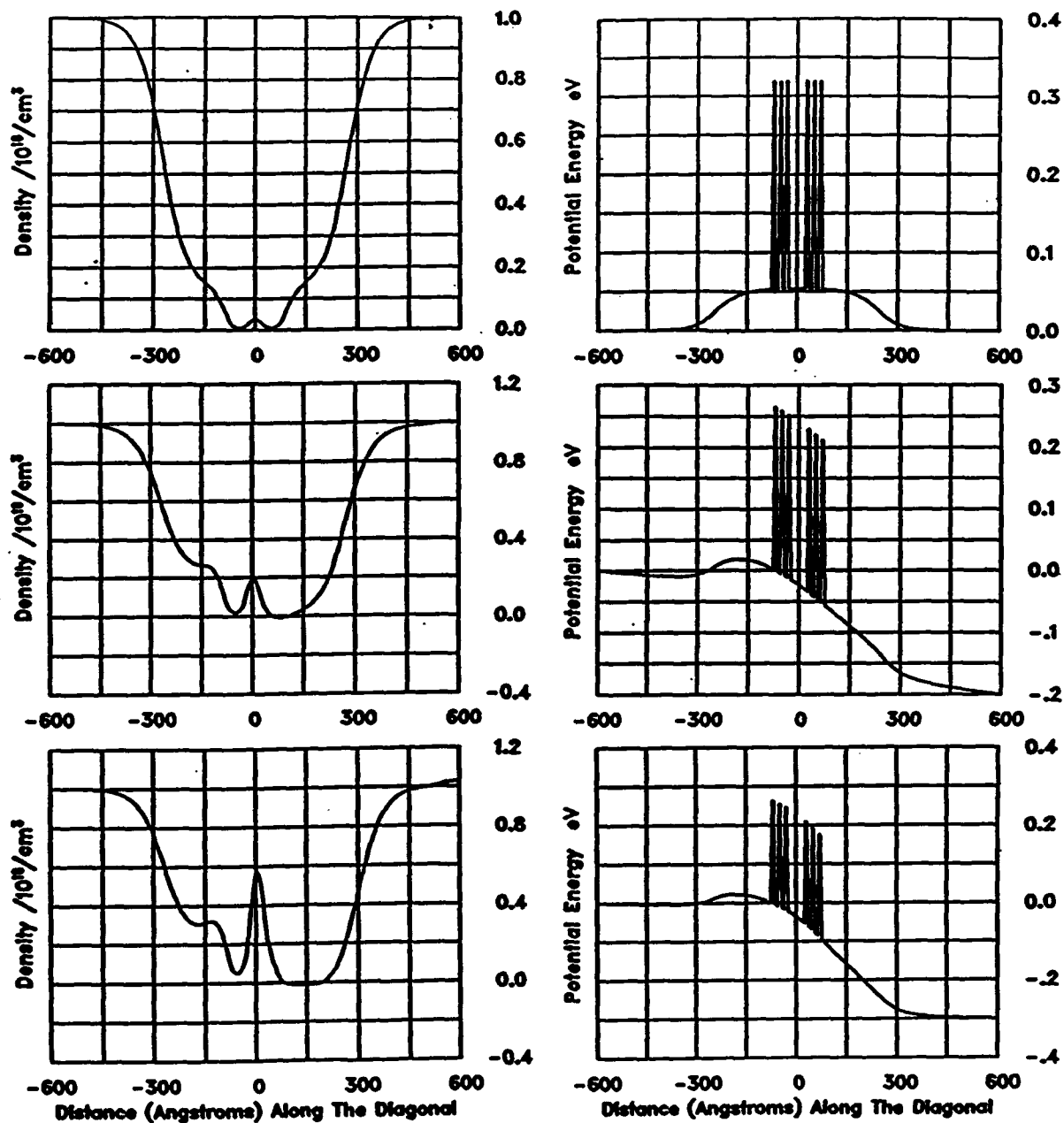
Figure 12. Density and potential energy distribution for the RTD structure with an N⁻ region of 500Å, at the indicated bias levels.
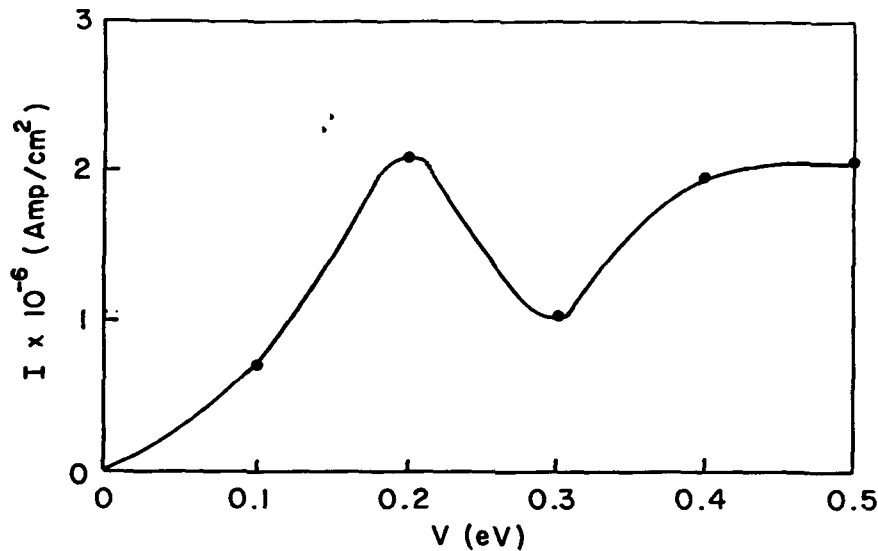
Figure 13. Current voltage characteristic for the calculations of figure 12.

notch potential. The current voltage characteristics for this structure are shown in figure 13, and yield a larger peak to valley ratio of 2.

Qualitative Dependence of RTD Operation on Scattering

The presence of negative differential conductance is clear from the above calculations. However, the details of the calculations are likely to depend upon the details of scattering within the structure studied. For example if at a certain carrier density the electrons undergo either strong electron-electron interaction or electron phonon interaction, and relax to a distribution with a local electron temperature and Fermi energy, then a variety of events can occur. One such case is that in which the local carrier density relaxes to a reduced Fermi energy within the quantum well. This has been modelled phenomenologically for the narrow N⁻ structure, through a variation in the Fermi energy in the vicinity of the double barriers. The resulting distribution of charge in the quantum well is shown in figure 14 at a bias level of -300 mev. Referring to the calculations of figures 8 through 11, which are characterized by a increasing charge in the quantum well, the calculation of figure 14 displays a charge distribution within the well that is of the order of that for the -200 mev calculation assuming only Fokker Planck scattering, and is less than the charge in the well at -300 mev assuming only FP scattering. There is also a further decrease in the current level for this calculation, indicating that the peak to valley ratio increases from 1.4 to 1.7. The above picture assumes that strong carrier relaxation occurs only after a sufficiently large number of carriers have accumulated in the quantum well.
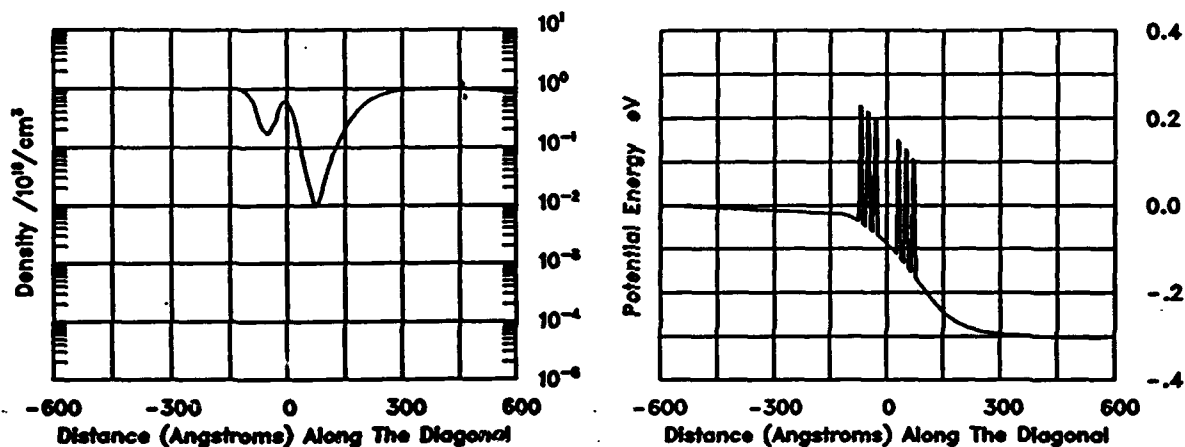
Figure 14. Distribution of charge and potential at -300 mev, assuming carrier relaxation within quantum well and a quasi-Fermi energy below that of the emitter.

Digression

Before continuing the discussion it is important to digress and emphasize that the calculations being performed are for structures with dissipation. Thus we are computing the real and imaginary parts of the density matrix, with the real part providing the density and the imaginary part providing the current. Our experience in performing these calculations is that any given charge distribution obtained from the full density matrix calculation, can be obtained ignoring the imaginary part, with a judicious choice of values of the quasi-Fermi energy. This particular feature has enabled us to explore a wide range of charge and potential distributions, prior to performing calculations with the full density matrix. Computing the full density matrix requires more resources than were available during this Phase I study; thus a number of calculations were performed using only the real part of the density matrix. To illustrate the effectiveness of this approach we repeat the figure 8 calculation, setting the imaginary part of the density matrix to zero. Figure 15 represents the result of this computation in which Σ_f is zero up to the second barrier, where upon it drops linearly across the second barrier until it reaches a value equal to the applied bias. The distribution of charge in figure 15 is nearly the same as that of figure 8. With respect to the potential drop, if we ignore differences in the cladding region, we see a qualitative similarity in potential drop.

The behavior discussed in figure 15, has been implemented for a number of

different problems with the same conclusion be drawn. As a result during this Phase I study calculations involving only the real part of the density matrix were used for preliminary studies when both electrons and holes were present. This is considered next.
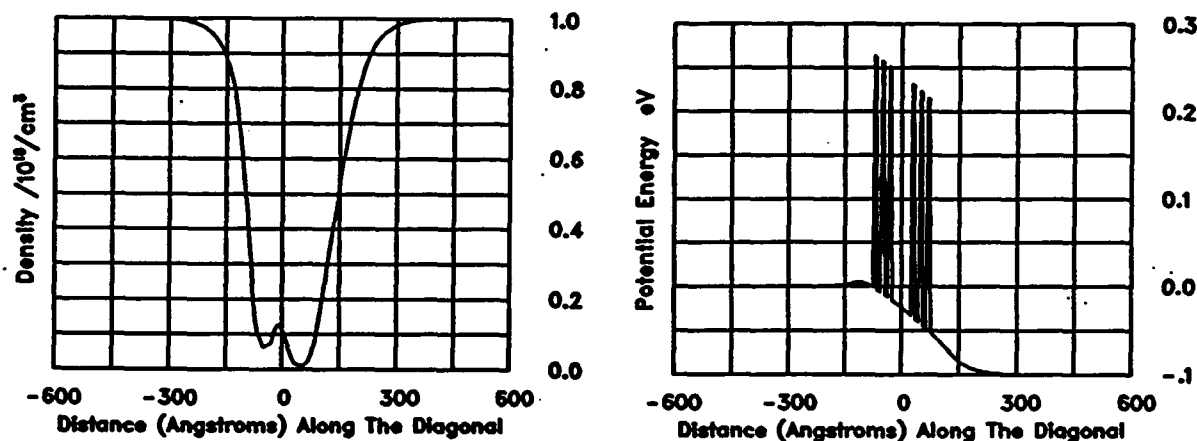

Figure 15. Potential and charge distribution for a calculation similar to figure 8, in which the imaginary part of the density matrix is negligible, and the density distribution is obtained by varying the quasi-Fermi energy as described in the text.

Calculations of the Real Part of the Density Matrix; Electrons and Holes

The calculation of figure 9 was repeated incorporating electrons and holes, as shown in figure 16. As discussed above, in this calculation the imaginary part of the density matrix is zero. Instead for both electrons and holes in which the quasi Fermi level, Σ_{fh}, of holes differs from that of electrons by the band gap energy, we computed the charge and potential distribution. The bias is -200 mev. The quasi-Fermi level is zero to the second barrier at which point it drops linearly to -200 mev at the end of the second barrier, and remains at that value until the end of the structure. The calculation displays a larger density of electrons in the quantum well than in those calculation in which dissipation is absent, but the general form is similar. Note the increased concentration of holes at the end of the second barrier, as well as the depletion of holes from the quantum well. The result is consistent with the quasi equilibrium conditions.
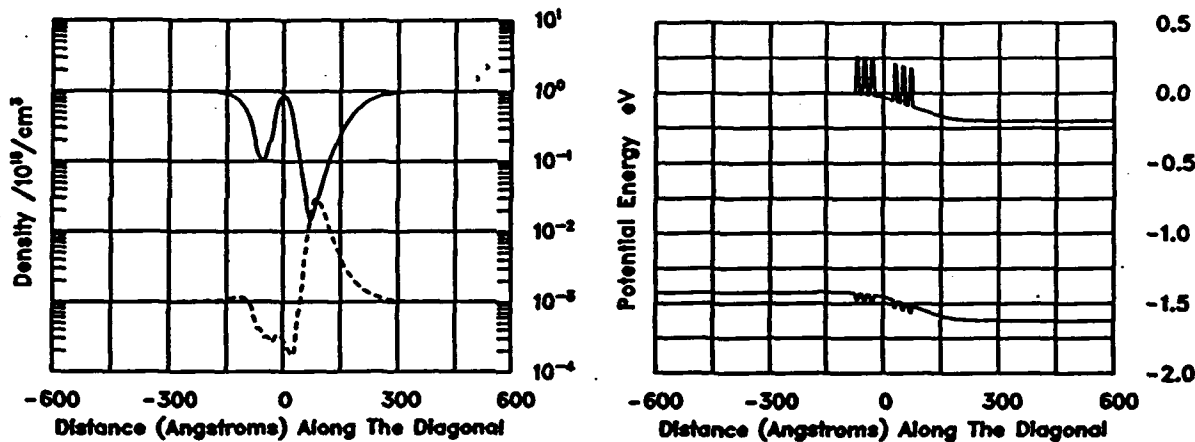
Figure 16. Potential and electron and hole charge distribution for a calculation similar to figure 8, in which the imaginary part of the density matrix is zero, the bias is -200 mev, and the density distribution is obtained by varying the quasi-Fermi energy as described in the text.

The situation at higher bias is considered in figure 17, where a bias of -300 mev is imposed. As in the earlier studies when holes were not part of the computation, we see in figure 17 an increase in electrons in the quantum well and a corresponding decrease in holes. However within, and downstream of the second barrier, there is an increased accumulation of holes. In a calculation in which holes are present in sufficient number, there can be a significant alteration of the potential distribution within and downstream of the second barrier. Indeed the potential distribution could yield flat band conditions sooner in the collector region, which would alter the predicted current voltage characteristics.

In discussing the role of scattering on the distribution of carriers in the structure, we pointed out that there could be significant alterations in the charge density depending upon the nature of the scattering events. We displayed, in figure 14, the situation when a large fraction of carriers were purged from the quantum well. A very similar calculations was performed for the case when holes were included. The calculations were performed at -300 mev. The structure is that of figure 14, in which the N⁻ region was taken to be 250 Å long. These results are displayed in figure 18, also for a bias of -300 mev. Comparing figures 17 and 18, we see for the latter a reduction of hole density within the second barrier, and a corresponding increase in

electron density. There is also an increase in hole density in the quantum well and a corresponding decrease in electron density in the quantum well.
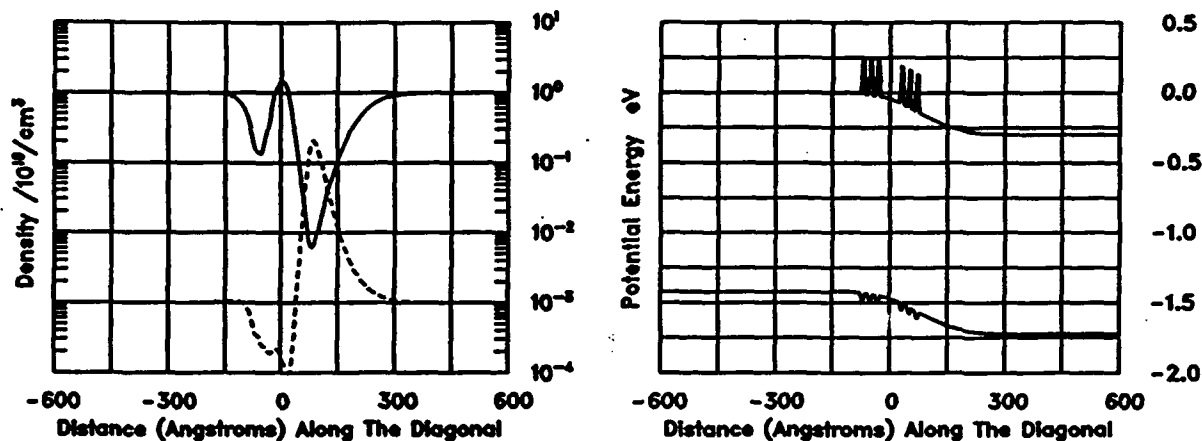
Figure 17. Potential and electron and hole charge distribution for a calculation similar to figure 16, in which the imaginary part of the density matrix is zero, the bias is -300 mev, and the density distribution is obtained by varying the quasi-Fermi energy as described in the text.
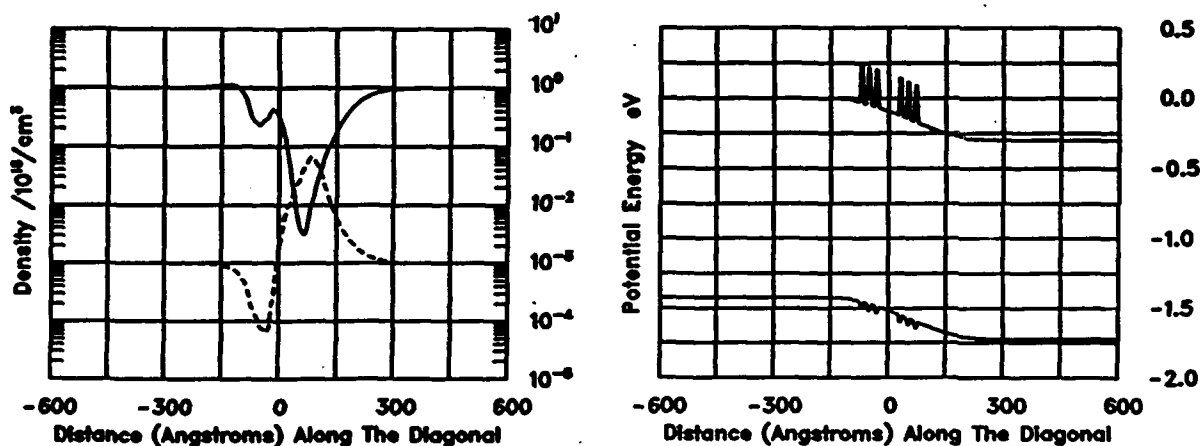
Figure 18. Distribution of charge and potential for a bias of -300 mev, assuming quasi-Fermi energy within the well that is below that of the emitter.

RESONANT TUNNELING GaAs/AlAs STRUCTURES: TRANSIENTS

Time dependent calculations were performed to determine the switching times in going from one configuration to another. The switching times are composed of two contributions, a tunneling contribution and a capacitive contribution. In the problem studied, which involves multiparticle behavior, no effort was made to identify each component. Capacitive (or displacement current) effects arise because of the inclusion of Poisson's equation. Several calculations were performed as described below.

Nonequilibrium Electrons

For this calculation the AlAs/GaAs structure was subject to a bias of -50 mev. The initial state was obtained from a quasi-Fermi level that was zero to the second barrier and varied linearly across the second barrier until reaching the value of -50 mev, at which point it was held constant until the collector boundary was reached. The final state was one in which the quasi-Fermi level was zero to the first barrier and then varied linearly across the double barrier region until reaching the value of -50 mev, at which point it was constant to the collector boundary. In the initial state there was a larger amount of charge in the well than at the final state. Both the initial charge distribution and the final charge distribution satisfied the constraint: $\int dr \rho_0(r) = N =$ constant. Clearly we are dealing with a tunneling problem.

Figure 19a shows the charge distribution at three instants of time; figure 19b shows the potential distribution. *The calculation indicates that the time duration in going from the initial to the final state is approximately 800 femtoseconds.* While changes in the potential distribution are obtained through solutions to Poisson's equation, coupled to the equation of motion of the density matrix, and so permit an evaluation of capacitive contributions, the potential variation is small and is not displayed here. Only the initial state is displayed. Figure 19c, displays the particle current as a function of position at two instants of time. Unlike the steady state case in which the particle current is spatially independent, here the spatial dependence is apparent. When combined with the term $\partial \rho / \partial t$, the total current, displacement plus particle current is *zero*, as it should be. The spatial variation suggests strong displacement current contributions away from the barriers.

Nonequilibrium Electrons and Holes

A very similar calculation was performed with holes included. As in the case of the electron calculation particle conservation was one of the constraints, in this case for both electrons and holes. Here again electrons tunnel out of the quantum well,

while holes tunnel through the barriers into the well. Recalling that the electrons and holes are coupled only through Poisson's equation, it is found that the holes are near equilibrium after 500 fs, which is considerably shorter than that of the electrons , which requires the same 800 fs discussed above.
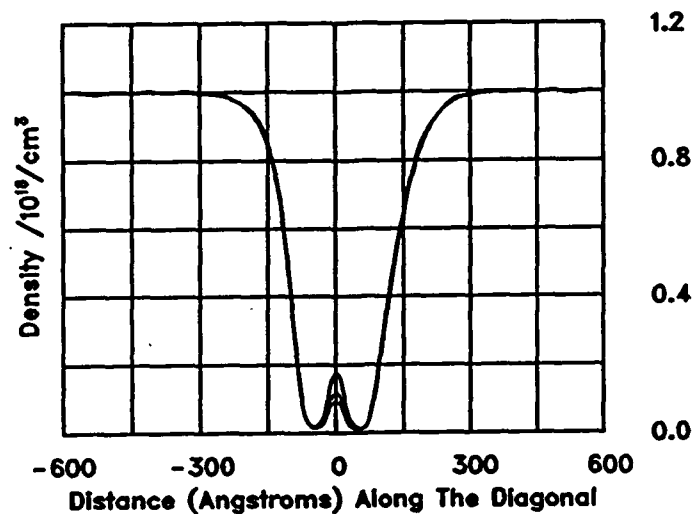

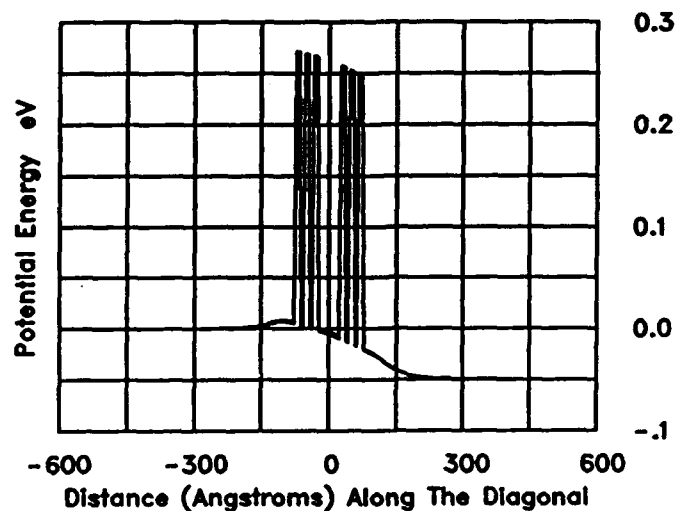*Figure 19a. Distribution of charge at three instants of time.*

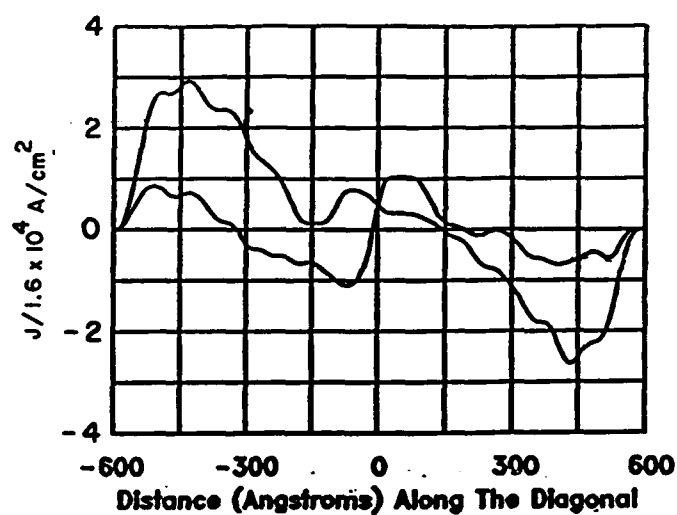*Figure 19b. Initial distribution of potential energy.*

Figure 19c. Distribution of particle current through the device at two instants of time.
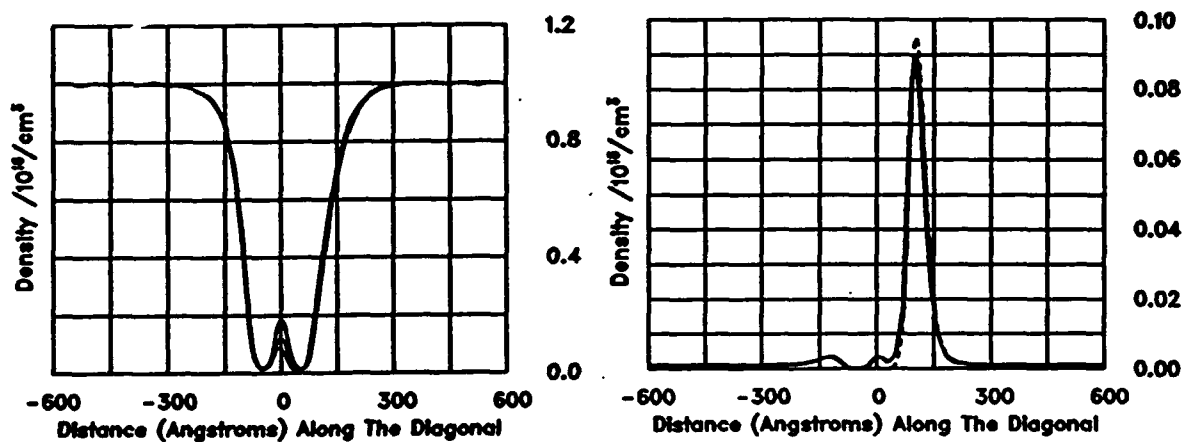

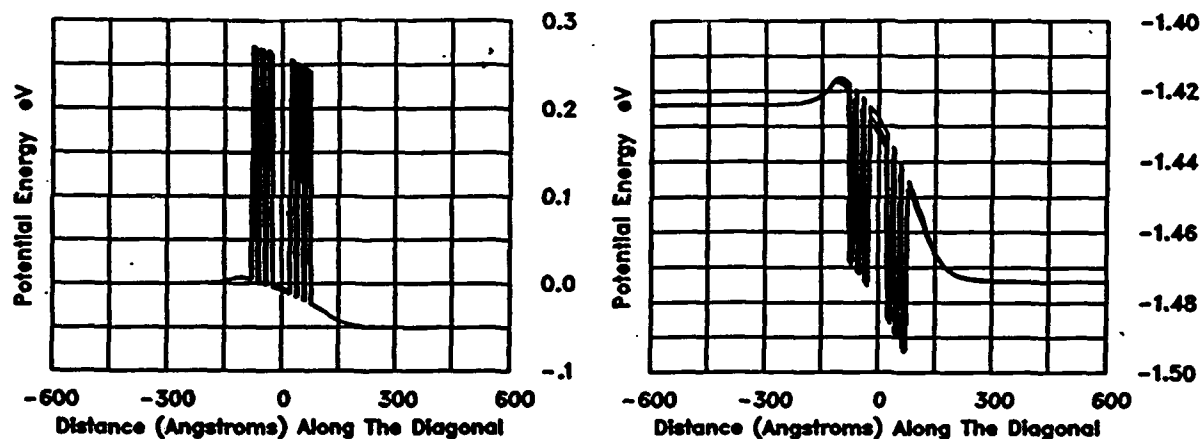*Figure 20a. Distribution of electrons and holes at three instants of time.*
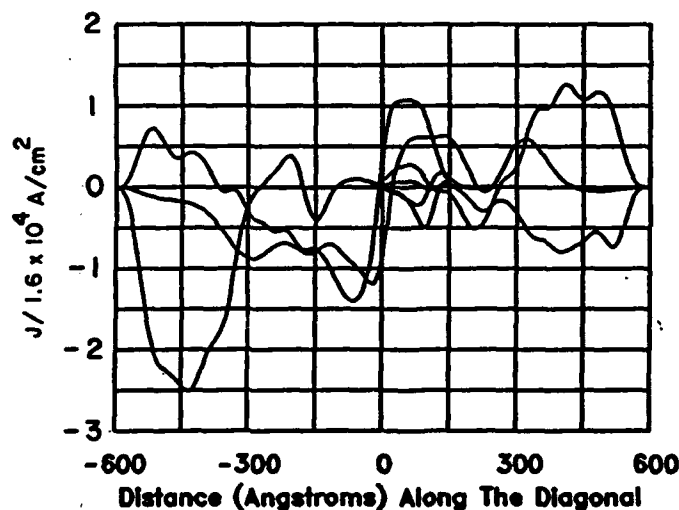
Figure 20b. *Initial distribution of potential energy.*

Figure 20c. *Distribution of particle current through the device at two instants of time.*

Transient Switching From One State to The Next

One of the objectives of the program was to go from one steady state to another and to calculate the current transient. The analysis was to include scattering, as well. Transient calculations with scattering are not complete, instead we invoked the different states using the earlier discussion associated with figures 14 through 18, where we introduced quasi-Fermi levels to account for scattering effects. The

resulting time dependent results require the inclusion of the imaginary parts of the density matrix; but this was done without dissipation.

The first calculation identified in figure 21, is for a condition in which the initial state is characterized by a bias of -100 mev, and the final state is equilibrium. Initially, the peak charge density in the well is approximately $4 \times 10^{17}/cm^3$ while the final state is approximately $9 \times 10^{16}/cm^3$. After 1.0ps the electron charge distribution reached approximately $1.4 \times 10^{17}/cm^3$, leading to the assumption that it would take approximately 2 ps to relax to equilibrium. It is estimated that including the scattering events would reduce the time to relaxation.

Figure 21, shows the electron and hole distribution at the indicated times. For this calculation the hole distribution shows an increase value in the collector barrier at the higher bias levels. This charge tunnels into the quantum well for the lower bias case. While it may appear that the holes relax sooner than the electrons, the time to steady state is governed by the slowest carrier transient.
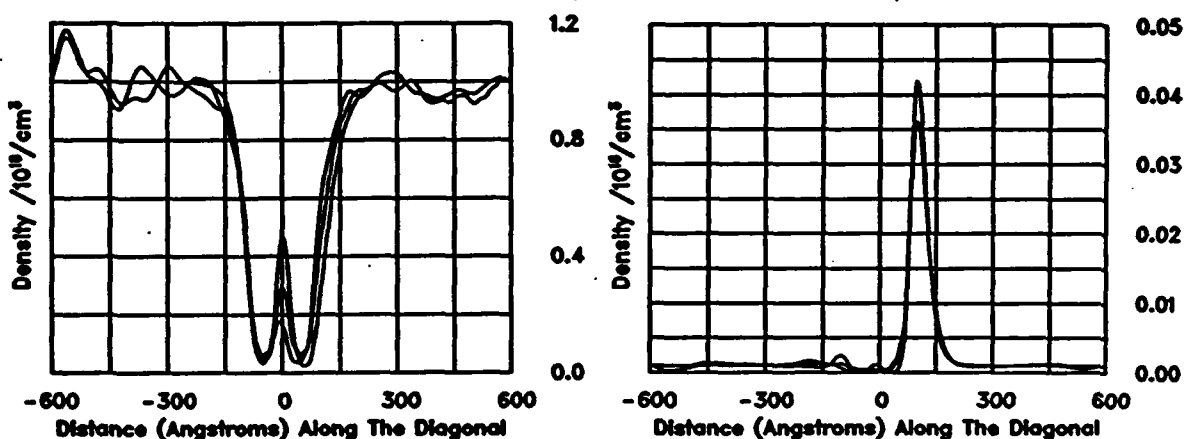

Figure 21. Electron and hole distribution at the indicate times for an RTD going from -100 mev to 0 mev.

Figure 22 shows the result using the same model as that of figure 21 for the case in going from -200 mev to - 300 mev. Thus for the case in which scattering was included we are going from a situation in which charge is in the well to the case where charge disappears from the well. The electron distribution after one picosecond is displayed in figure 22, where it is seen that after this period of time the electron distribution has not relaxed to steady state. It may take as long as two to three picoseconds before all of the charge is cleared from the structure. The holes while initially strong within the collector barrier show a steady decrease as time progress, but a steady state has not been reached.
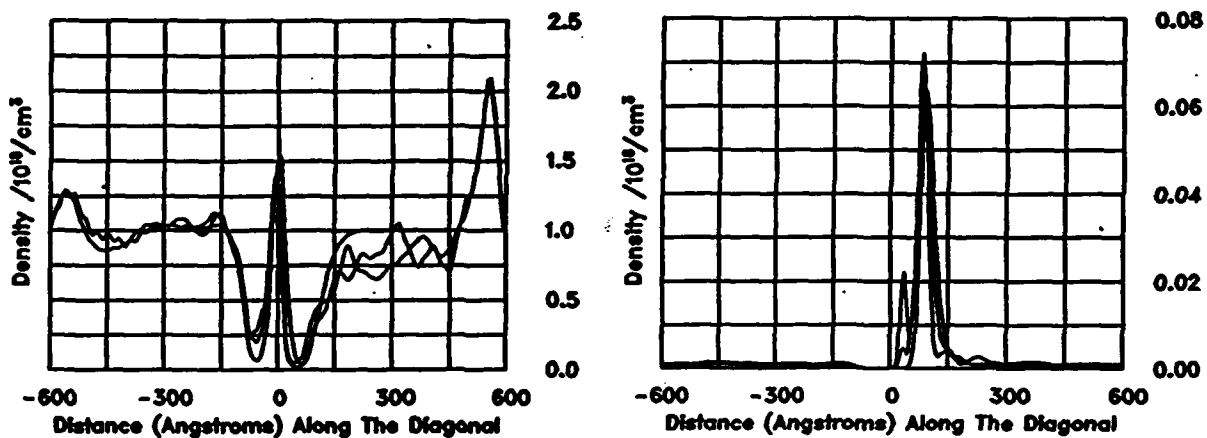

Figure 22. Electron and hole distribution at the indicate times for an RTD going from -200 mev to -300 mev, assuming scattering within the quantum well that result in the carriers leaving the well.

RESONANT TUNNELING II-VI STRUCTURES: STEADY STATE

Double barrier calculations were performed for a structure consisting of a CdTe barrier, and a $Hg_{0.78}Cd_{0.22}Te$ quantum well. The effective mass of the electrons was taken as $0.015m_e$. We point out that this structure exhibited negative differential resistance at 4 K for a single barrier with the negative resistance thought to arise because the electron tunneling probability is reduced as the valence band edge in the barrier is pushed to lower energies by an increasing applied voltage (Chow et al, 1988). In the present study we concentrated on electron transport through two barriers at room temperature. While we have begun to examine transport in structures at temperatures near 4 K, with incorporation of the Pauli exclusion principle, the calculations performed during the Phase I study were room temperature calculations. *Negative differential resistance was not observed.* The doping for this structure was similar to that of the AlAs/GaAs structure with the N⁻ region being 500 Å long. The barriers were taken to be 1.4 ev high. The barrier and well widths were 70 Å each.

The equilibrium distribution of electrons and potential energy are shown in figure 23. There is considerable depletion in the vicinity of the barriers, more than that of the AlAs barriers, but the charge density in the center of the quantum well is approximately equal to that of the AlAs/GaAs structure considered earlier.

As the bias is increased to -100 mev, figure 24, there is a small amount of charge accumulating on the emitter side of the first barrier, some enhanced charge depletion on the collector side of the second barrier and an increase in charge in the quantum well. The charge within both barriers decreases. The situation at -200 mev and -300 mev are shown in figures 25 and 26. There is further increases in charge within the quantum well, further movement of the depletion layer toward the collector side of the structure. But unlike the AlAs/GaAs study, there is very little pinning of the emitter barrier. Negative conductance was not observed at the bias levels considered. Negative conductance, if present, would occur at an estimated bias level of -800 mev, where the resonant level of approximately 250 mev would be in the vicinity of the emitter Fermi level. The structure studied was not long enough to permit a realistic assessment of this contribution. Continuation of this study for longer structures is anticipated as part of a Phase II study.
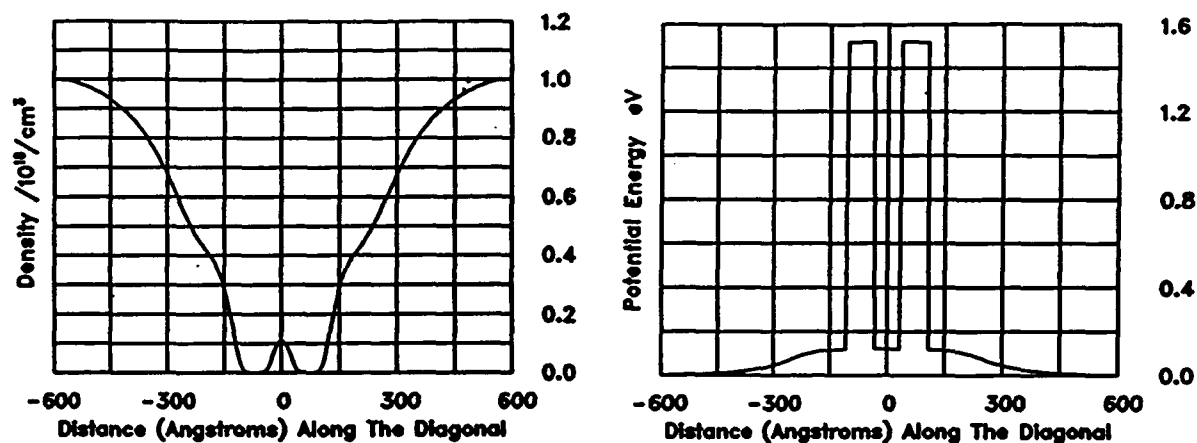
Figure 23. Equilibrium characteristics for a II-VI double barrier structure.
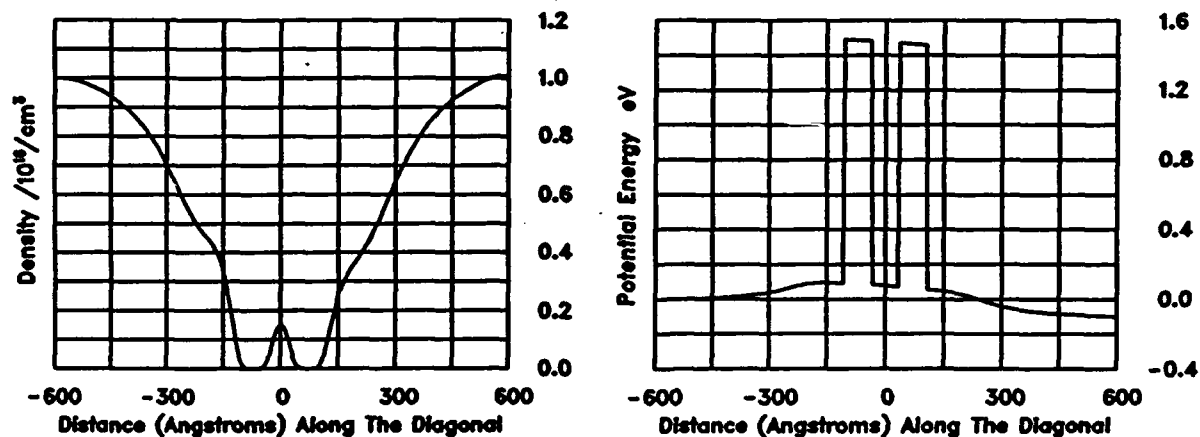

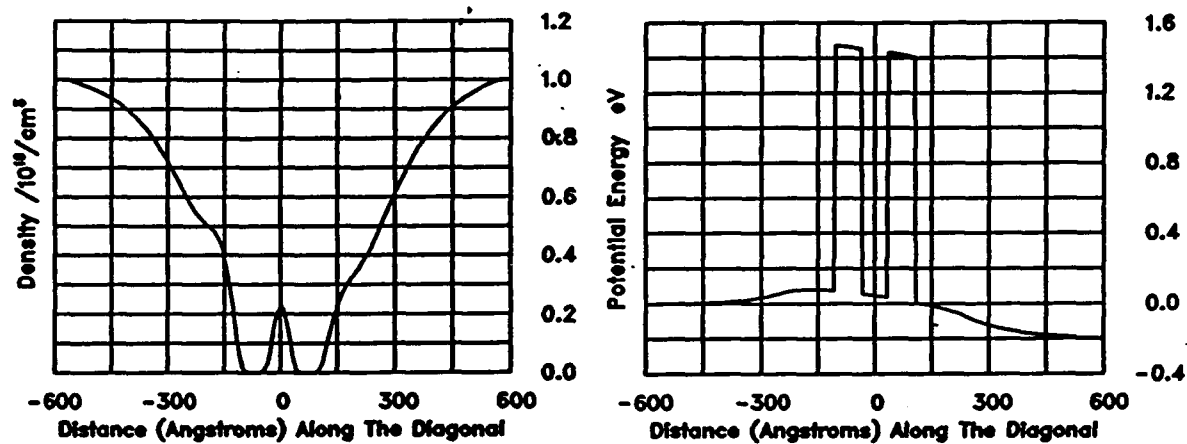Figure 24. Density and potential distribution for the figure 23 structure at -100mev.

Figure 25. Density and potential distribution for the figure 23 structure at -200mev.
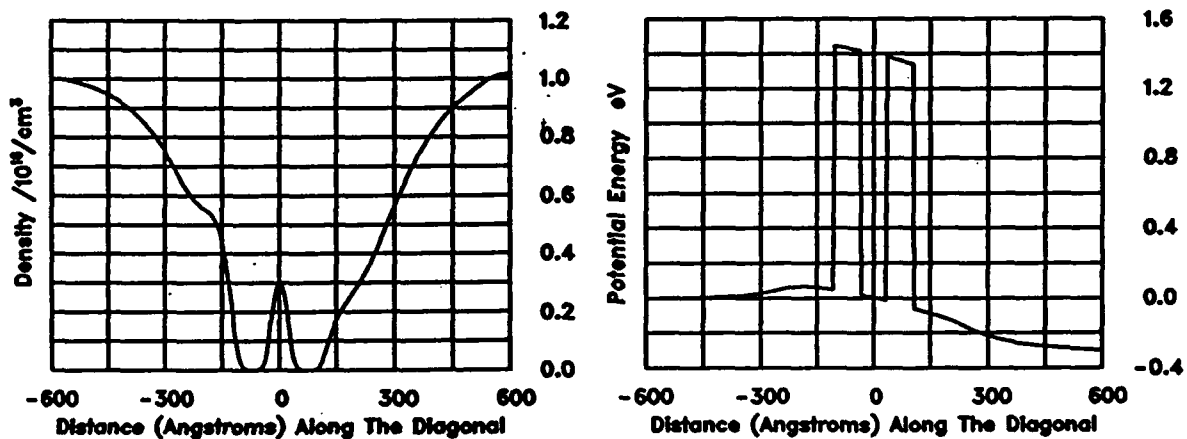

Figure 26. Density and potential distribution for the figure 23 structure at -300mev.

MISCELLANEOUS ELECTRON AND HOLE CALCULATIONS

The ability to treat both electron and hole transport in quantum structures is necessary for a full understanding of the operation of these structures. For while structures can be defined in which the numbers of holes contributing to transport is small, in regions where the numbers of electrons and holes are nearly equal, differences in their values can have a strong influence on the local potential drop and will affect the current flow through the structure. It is therefore useful to demonstrate that the Liouville equation is capable of dealing with a number of disparate problems. This section illustrates some additional capability. All calculations in this section are equilibrium calculations.

PN Junction

As in the section on AlAs/GaAs we begin with a discussion of doping variation. Figure 27 displays the solution to the Liouville equation for a PN junction. The results look classical, but as additional analysis (not shown) indicates there are quantum contributions associated with the gradient changes in the density which lead to changes in energy of the order of several mev in the junction regions. For this calculation the electrons and holes were taken to have the same effective mass. As a result the distributions of the carriers are symmetric.
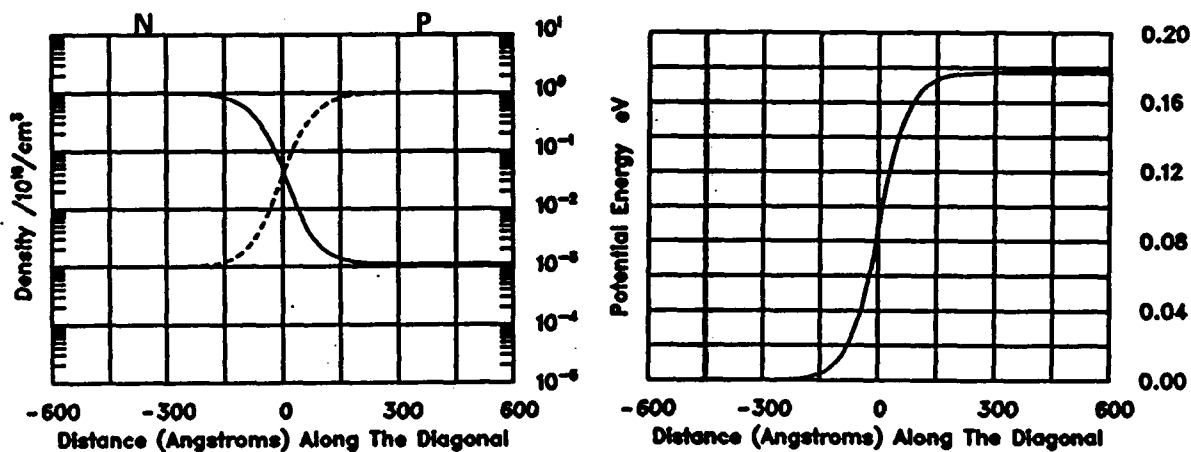

Figure 27. Distribution of electrons, holes and potential energy for a PN junction at equilibrium.

NPN Structure

This calculation is germane to the calculations of the earlier section. Again we are assuming that the effective mass of the holes and electrons are equal. The distribution of carriers is displayed in figure 28. Note for this structure there is a decrease in the electron density within the P region. The density of carriers is below that associated with the N⁻ region of the earlier calculations, and the potential barrier reaches a height of nearly 150 mev. Recall that the potential barrier of the N⁻ structure was approximately 50 mev. The quantum contributions to the potential barrier for the NPN structure are of the order of 15 mev for the electrons and 5 mev for the holes.
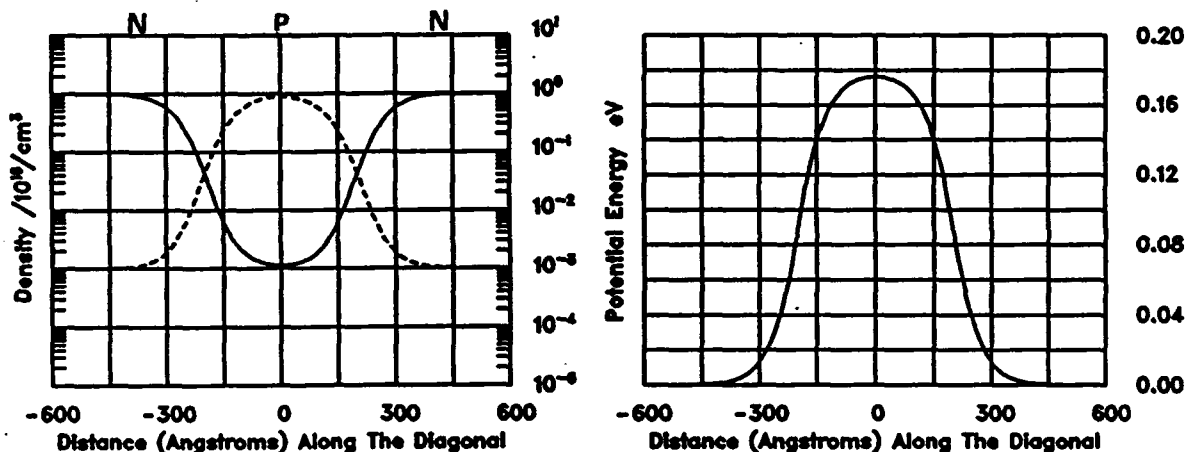

Figure 28. Distribution of electrons, holes and potential energy for an NPN junction at equilibrium.

Type I and Type II Single Barrier Structures

The discussion of the earlier sections has been confined to type I structures. Here a barrier for electrons is coupled to a barrier for holes. The inverted, or type II structure is one where a barrier for electrons is coupled to a well for holes. The donor concentration for this calculation is the same as that of figure 4, whereas the acceptor concentration is uniform and three orders of magnitude below the donor concentration.

In figures 29 and 30 we display single barrier type I and type II structure calculations. For these calculations the effective masses of electrons and holes were equal. The

point to note is that for the type I barrier there is a depletion of holes within the barrier region, whereas for the type II barrier there is a local accumulation of holes. Note in the case of the type II barrier, the local density of holes in the barrier exceeds that of the electrons. There is no significance to the value of the bandgap.
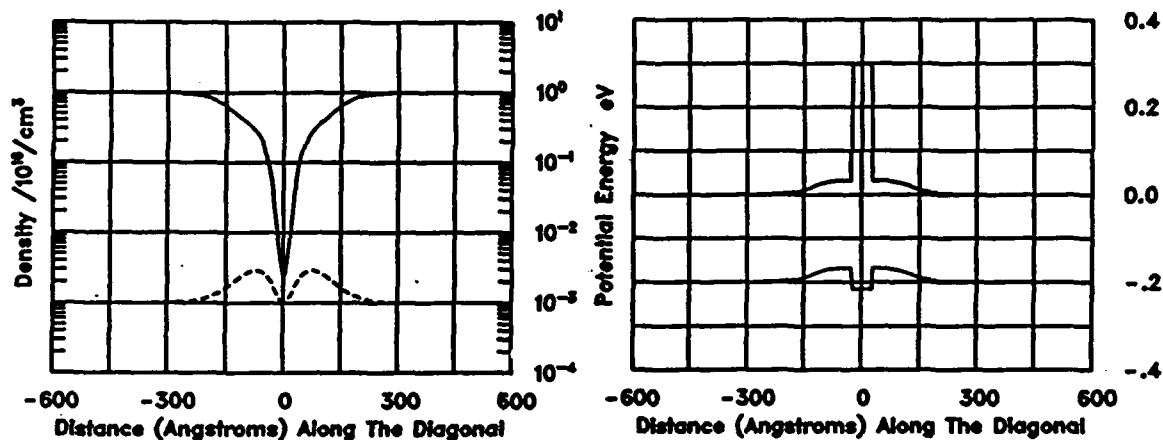

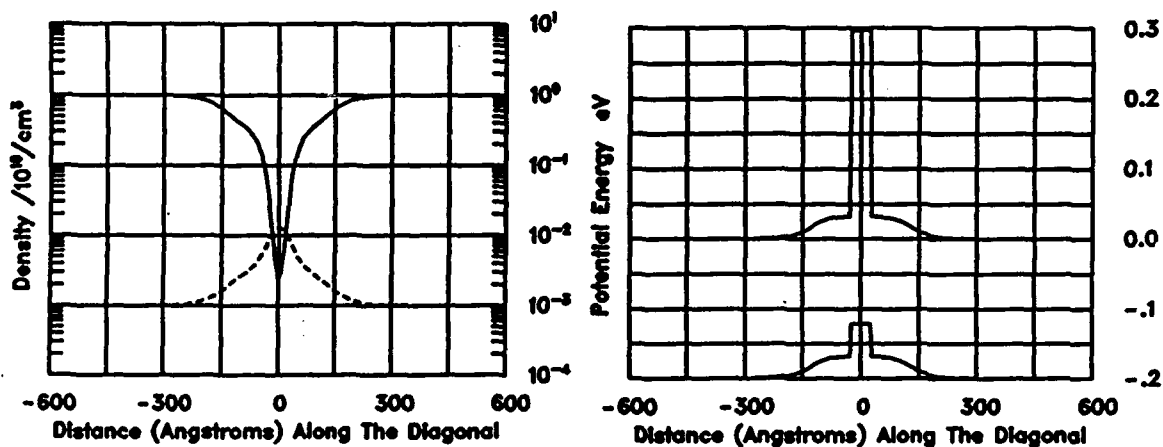*Figure 29. Electron, hole and potential distribution for a type I barrier under equilibrium.*

Figure 30. Electron, hole and potential distribution for a type II barrier under equilibrium.

Type I and Type I Double Barrier Structures

The double barrier type I structure was studied in detail in the earlier sections. We display below calculations with a type II structure, and for comparison a type I structure. The doping concentration is the same as figures 29 and 30. The important *difference* to note between the type II and type I structures is the accumulation of holes in the barrier regions, and as a consequence there is a *greater accumulation of holes in the quantum well when compared to the type I structure.*
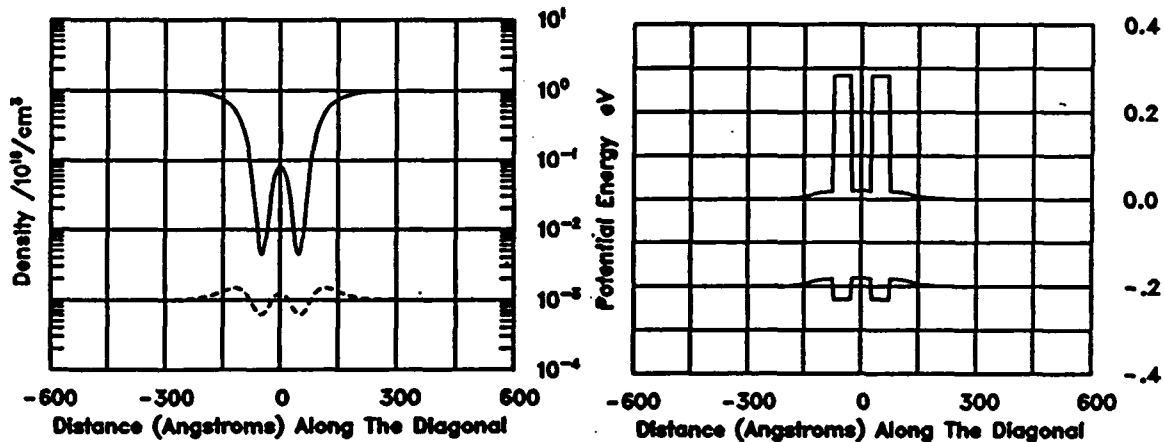
Figure 31. Electron, hole and potential distribution for a type I double barrier structure under equilibrium.
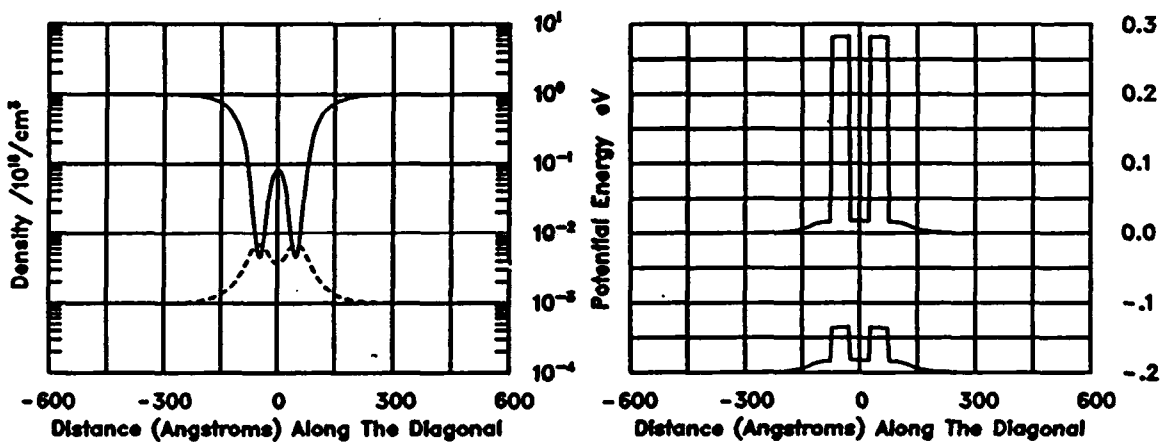
Figure 32. Electron, hole and potential distribution for a type II double barrier structure under equilibrium.

THE NUMERICAL PROCEDURE

Equivalent first order systems of equations have been derived for the equation of motion of the density matrix and these systems are solved. Typical solutions, require about 20 seconds of Cray-XMP CPU time demonstrating the efficiency of the procedure. A typical first order system, *without dissipation* is:

$$(14) \qquad u(x,x') + [i\hbar/2m][\rho_x + \rho_{x'}] = 0, \qquad \rho_t + [u_x - u_{x'}] + [i/\hbar][V(x,x't)]\rho = 0$$

where $V(x,x't) = V(x,t) - V(x't)$. The characteristic directions for the system of equations (15) are: $\eta = (x + x')/2 = \text{constant}$, $\zeta = (x-x')/2 = \text{constant}$. In terms of the characteristic directions η and ζ, equations (14) are written as:

$$(15) \qquad u(x,x') + [i\hbar/2m]\rho_\eta = 0, \qquad \rho_t + u_\zeta + [i/\hbar][V(x,x',t)]\rho = 0$$

Suitable boundary conditions for equations (15) are the specification of ρ and u along the boundary $x' = 0$ and the specification of u along the boundary $x = L$, where L is the length of the device. Along the boundary $x = 0$, ρ is specified as the complex conjugate of $\rho(x,0)$, since ρ is Hermitian, and u is computed from the outgoing characteristic equation (15b). Along the boundary $x = L$, ρ is computed from the outgoing characteristic equation (15a). The overall solution procedure consists of solving the equations as an initial boundary-value problem starting from conditions along the line $x' = 0$ and marching to the line $x' = L$ using the method of characteristics. A characteristic net for the equation of motion of the density matrix is constructed a-priori from grid points of a uniform square grid. A discrete form of equations (15) can be written on this grid as

$$(16a) \qquad [u]_{av} + [i\hbar/2m][\rho(i,j) - \rho(i-1,j-1)]/\Delta\eta = 0$$

$$(16b) \qquad [\rho_t]_{av} + [u(i+1,j-1) - u(i,j)]/\Delta\zeta + [i/\hbar][V(x,x',t)]_{av}[\rho]_{av} = 0$$

where $[\cdot]_{av}$ represents an average over the grid cell. Depending upon the form of averaging chosen, equations (16) form a system of 2x2 block tridiagonal or block diagonal algebraic equations that can be solved at $x' = j$ from known values at $x' = j-1$. Thus, the solution procedure can be marched from boundary conditions at $x' = 0$, in steps along x', to $x' = L$. Self-consistency is included in the analysis by iterating the solution of the density matrix with the solution of Poisson's equation to convergence.

SUMMARY

The Phase I study represents a major advance in the study of transients in quantum structures. Both electrons and holes were examined, and both the tunneling and capacitive contributions were determined to yield a characteristic time of the order of one picosecond.

There is still algorithm work to be done. The algorithm must incorporate more realistic scattering mechanisms, and transients including dissipation must be addressed. This feature is an ongoing part of the SRA quantum transport programs.

It is anticipated that within the next quarter, spatially dependent effective masses will be included in the study as well as Fermi statistics at room temperature. Fermi statistics at 0 K is part of the algorithm. The algorithm discussed here is capable of treating a broad range of devices, both one and two dimensional, as well as quantum wires, and will provide a major advance in understanding the operation of quantum structures.

APPENDIX: THE SCATTERING INTEGRALS

The approach we have taken is to start from the classical scattering integral and then introduce the density matrix through the Wigner-Weyl transformation. Strictly, this approach is only correct for the situation when the distribution functions are probabilities. Thus it is not correct for the Wigner function. In the discussion that follows we will be seeking the classical form of the scattering terms as they apply to the equation of motion of the density matrix in the coordinate representation. Intuitive arguments will be invoked to introduce some quantum contributions to these scattering terms. A more general approach is under investigation.

The standard scattering integral within the framework of the Boltzmann equation is:

(A.1) $[\partial f / \partial t]_{scattering} =$

$-[2\Omega/(2\pi)^3][_{-\infty}\int^{+\infty}dk'\{f(k,x)\{1-f(k',x)\}W(k,k')-f(k',x)\{1-f(k,x)\}W(k',k)\}$

where as indicated above the distribution function must represent a probability. Note: dk denotes a three dimensional integration. If the density of particles is low enough such that we can ignore Fermi statistics, equation (A.1) simplifies:

(A.2) $[\partial f / \partial t]_{scattering} =$

$= -[2\Omega/(2\pi)^3][_{-\infty}\int^{+\infty}dk'\{f(k,x)W(k,k')-f(k',x)W(k',k)\}$

We now use the Weyl transformation as exemplified by equation (10) for the specific case where the Liouville potential is dependent only on the coordinates x and x'; i.e., it is independent of the pairs (y,y') and (z,z'). Using the Weyl transformation, the scattering integral becomes:

(A.3) $[\partial f / \partial t]_{scattering} = -[2\Omega/(2\pi)^3][1/(2\Omega)][_{-\infty}\int^{+\infty}dk'd^3\xi\,\rho(x+\xi/2,x-\xi/2)$

$X\,[exp[-ik\cdot\xi]W(k,k')-exp[-ik'\cdot\xi]W(k',k)]$

In terms of the density matrix, another application of the Weyl transformation yields:

(A.4) $[\partial\rho/\partial t]_{scattering} = -[2\Omega/(2\pi)^6][_{-\infty}\int^{+\infty}dk'dkd^3\xi\,\rho(x+\xi/2,x-\xi/2)exp-[ik\cdot\xi]$

$X\,W(k,k')\{exp[2ik\cdot\varsigma]-exp[2ik'\cdot\varsigma]\}$

Equation (A.4) is rewritten in the following manner:

(A.5) $[\partial \rho/\partial t]_{\text{scattering}} =$

$-[2\Omega/(2\pi)^6][_{-\infty}\int^{+\infty}dk'dkd^3\xi\,\rho(x+\xi/2,x-\xi/2)\exp-[ik\cdot(\xi-2\varsigma)]W(k,k')$

$$x\{1-\exp[+2i(k'-k)\cdot\varsigma]\}$$

$=-[2\Omega/(2\pi)^6][_{-\infty}\int^{+\infty}dk'dkd^3\xi\,\rho(x+\xi/2,x-\xi/2)\exp-[ik\cdot(\xi-2\varsigma)]W(k,k')$

$$x\{1-\cos[2(k'-k)\cdot\varsigma]\}$$

$+[2\Omega/(2\pi)^6][_{-\infty}\int^{+\infty}dk'dkd^3\xi\,\rho(x+\xi/2,x-\xi/2)\exp-[ik\cdot(\xi-2\varsigma)]W(k,k')$

$$x\{i\sin[2(k'-k)\cdot\varsigma]\}$$

We concentrate on the second part, and deal with polar phonon scattering, which requires that $k'\sim k$ (see Hess). For this case the second part of equation (A.5) can be written as:

(A.6)

$+[2\Omega/(2\pi)^6][_{-\infty}\int^{+\infty}dk'dkd^3\xi\,\rho(x+\xi/2,x-\xi/2)\exp-[ik\cdot(\xi-2\varsigma)]W(k,k')\{i2(k'-k)\cdot\varsigma\}$

We now recognize an earlier result:

(A.7) $[2\Omega/(2\pi)^3][_{-\infty}\int^{+\infty}dk'W(k,k')(k-k')=k\Gamma(E)$

leading to the following form for equation (A.6):

(A.8) $-2i/(2\pi)^3[_{-\infty}\int^{+\infty}dkd^3\xi\,\rho(x+\xi/2,x-\xi/2)\exp-[ik\cdot(\xi-2\varsigma)]k\cdot\varsigma\Gamma(E)]$

where $\Gamma(E)$ denotes an energy dependent scattering rate. It is useful to note that it may be more relevant to use a dispersion relation in the expression for the scattering rate. That is $\Gamma(E)$ be replaced by $\Gamma(k)$.

For example, for bulk polar phonons,

(A.9) $\Gamma = \{\hbar eF_0/[2\surd(2mE)]\}\{N_q[\chi^+ -(\hbar\omega_0/E)\sinh^{-1}\surd(E/\hbar\omega_0)]$

$$(N_q+1)[\chi^- +(\hbar\omega_0/E)\sinh^{-1}\surd(E/\hbar\omega_0 -1)]\}$$

where:

(A.10) $\chi^{\pm} = \sqrt{(1 \pm \hbar\omega_0/E)}$

and F_0 is the Frohlich field.

We are going to concentrate on an evaluation of equation (A.8). First we recognize that equation (A.8) can be rewritten as $-\zeta \cdot \nabla_\zeta K_1$, where:

(A.11) $K_1 = [1/(2\pi)^3][_{-\infty}\int^{+\infty} dk d^3\xi \, \rho(x+\xi/2, x-\xi/2) \exp[-ik \cdot (\xi-2\zeta)]\Gamma(E)]$

We now evaluate equation (A.11). To facilitate this evaluation we introduce a change in variable through $\xi' = 2\zeta$. Then assuming an integration over spherical polar coordinates with the following directions:

(A.12) $k = (k, \alpha, \beta)$
$\xi = (\xi, \theta, \phi)$
$\xi' = (\xi', \theta', \phi')$

and

(A.13a) $\exp[ik \cdot \xi] = 4\pi\Sigma_{\ell=0,\infty}\Sigma_{m=-\ell,+\ell}[(i)^\ell j_\ell(k\xi) Y_\ell^m(\alpha,\beta)^* Y_\ell^m(\theta,\phi)]$

(A.13b) $\exp[ik \cdot \xi'] = 4\pi\Sigma_{\ell=0,\infty}\Sigma_{m=-\ell,+\ell}[(i)^\ell j_\ell(k\xi') Y_\ell^m(\alpha,\beta)^* Y_\ell^m(\theta',\phi')]$

Thus:

(A.14) $\exp[ik \cdot (\xi-\xi')] = (4\pi)^2\Sigma_{\ell,\ell'=0,\infty}\Sigma_{m,m'=-\ell,-\ell',+\ell,\ell'}$

$[(i)^\ell(-i)^{\ell'} j_\ell(k\xi) j_{\ell'}(k\xi') Y_\ell^m(\alpha,\beta) Y_{\ell'}^{m'}(\alpha,\beta)^* Y_\ell^m(\theta,\phi) Y_{\ell'}^{m'}(\theta',\phi')^*]$

Note that:

(A.15) $_0\int^{2\pi}{}_0\int^{\pi} \sin\alpha \, d\alpha \, d\beta \, Y_\ell^m(\alpha,\beta) Y_{\ell'}^{m'}(\alpha,\beta)^* = \delta_{m,m'}\delta_{\ell,\ell'}$

Inserting equation (A.15) into the scattering integral, equation (A.11) and integrating over the angular dependence of the wave vector k, we obtain:

(A.16) $K_1 = [2/\pi]\Sigma_{\ell=0,\infty}\Sigma_{m=-\ell,+\ell} Y_\ell^{m'}(\theta',\phi')$

$_{-\infty}\int^{+\infty} d^3\xi \, Y_\ell^m(\theta,\phi)^* \rho(x+\xi/2, x-\xi/2) \, _0\int^{+\infty} k^2 \, dk[j_\ell(k\xi) j_\ell(k\xi')\Gamma(k)]$

-53-

Note: when $\Gamma(k)$ is independent of k, the integration over k is direct and leads to:

(A.17) $\quad _0\int^{+\infty} k^2 dk j_\ell(k\xi) j_\ell(k\xi') = [\pi/2\xi^2]\delta(\xi-\xi')$

Thus:

(A.18) $\quad K_1 = \Sigma_{\ell=0,\infty} \Sigma_{m=-\ell,+\ell} Y_\ell{}^m(\theta',\phi')$

$\quad\quad _{-\infty}\int^{+\infty} d^3\xi\, Y_\ell{}^m(\theta,\phi)^* \rho(x+\xi/2,x-\xi/2)/\xi^2 \delta(\xi-\xi')\Gamma$

The summation, based upon completeness of the eigenfunctions yields:

(A.19) $\quad \Sigma_{\ell=0,\infty} \Sigma_{m=-\ell,+\ell} Y_\ell{}^m(\theta',\phi') Y_\ell{}^m(\theta,\phi)^* = \delta(\theta-\theta')\delta(\phi=\phi')$

and equation (A.18) becomes:

(A.20) $\quad K_1 = \rho(x+\xi'/2,x-\xi'/2)\Gamma = \rho(x+\zeta,x-\zeta)\Gamma$

Thus equation (A.20) for a constant relaxation time becomes:

(A.21) $\quad -\zeta \cdot \nabla_\zeta K_1 = -\Gamma\zeta \cdot \nabla_\zeta \rho(x+\zeta,x-\zeta)$

which has the same structure as the first term of the Fokker-Planck dissipation.

REFERENCES

- Bonnefoi, A. R., T. C. McGill and R. D. Burnham (1988), Phys. Rev. *B15-37*, 8754.
- Calderia, A. O. and A. J. Leggett (1983), Physica *121A*, 587.
- Capasso, F. and R. A. Kiehl (1985), A. Appl. Phys. *58*, 1366.
- Capasso, F., S. Sen, F. Beltram and A. Y. Cho, (1990), *Physics of Quantum Electron Devices*, Capasso, ed., 181.
- Chang, L. L., L. Esaki, and R. Tsu, (1974) Appl. Phys. Lett, *24*, 593.
- Chow, D. H., T. C. McGill, I. K. Sou, J. P. Faurie, and C. W. Nieh, Appl. Phys. Letts., *52*, 54.
- Dingle, R., W. Wiegmann, and C. H. Henry (1974) Phys. Rev. Lett. *33*, 827
- Dutta, M., K. K. Choi and P. G. Newman (1989) Appl. Phys. Lett. *55*, 2429.
- Feynman, R. P. (1972), *Statistical Mechanics* Benjamin, Reading
- Frensley, W. R. (1985)J. Vac. Sci. Technol., *B3*, 1261
- Frensley, W. R. (1990), Rev. Mod. Phys. *62*, 745.
- Govindan, T. R., H. L. Grubin and F. J. de Jong (1991), *Computational Electronics*, Hess, Leburton and Ravaioli, eds., Kluwar, 215.
- Grubin, H. L., T. R. Govindan and M. A. Stroscio, (1992) To be published.
- Heiblum, M. (1981) Solid State Electronics *24*, 343.
- Huang, C. I., M. J. Paulus., C. A. Bozada., S. C. Dudley, K. R. Evans, C. E. Stutz, R. L. Jones, and M. E. Cheney, (1987) Appl. Phys. Letts., *51*, 121.
- Kastalsky, A. and S. Luryi, (1983), IEEE Electron Dev. Letts. *EDL-4*,334.
- Linh, N. T. (1987), Semiconductors and Semimetals, R. Dingle, ed., pp. 203.
- Potz, W. (1989), J. Appl. Phys. *66*, 2458.
- Shaw, M. P., V. V. Mitin, E. Scholl and H. L. Grubin (1992) *The Physics of Instabilities in Solid State Electron Devices*, Plenum Press, NY
- Tsu, R. and L. Esaki (1973), Appl. Phys. Letts. *22*, 562.
- Wigner, E. P. (1932), Phys. Rev *40*, 749.